

Directional Freeze-Casting: A Bioinspired Method to Assemble Multifunctional Aligned Porous Structures for Advanced Applications

Mohammad-Ali Shahbazi, Masoumeh Ghalkhani, and Hajar Maleki*


Herein, the potential of directional freeze-casting techniques as a very generic, green, and straightforward approach for the processing of various functional porous materials is introduced. These materials include 3D monoliths, films, fibers, and microspheres/beads, which are obtained by the assembly of network building blocks originated from cryoassembly of the various aqueous-based systems. The process simply relies on 1) directional freezing of the slurry through contact with a cold surface, 2) maintaining the slurry at the frozen state for a particular time with controlling the freezing parameters and directions, and 3) sublimation of the created ice crystal templates inside the developed structure to translate the ice growth pattern to final porous structure. The materials developed with such a cryogenic process contain a highly complex porous structure, e.g., a hierarchical and well-aligned microstructure in different levels, which renders a high control over the physicochemical and mechanical functionalities. Due to the versatility and controllability of this technique, the process can also be extended for the mimicking of the structures found in natural materials to the bulk materials to assemble bioinspired porous composites with many useful mechanical and physical features. The aim, herein, is to give a brief overview of the recent advances in developing anisotropic porous inorganic, organic, hybrid, and carbonaceous materials with a particular emphasis on materials with biomimicking microstructure using directional ice templating approach and to highlight their recent breakthrough for different high-performance applications.

1. Introduction

Compared with the isotropic porous materials with randomly oriented porous and microarchitecture, materials with well-ordered pore morphology and aligned microarchitecture have shown outstanding improvement in some physicochemical and mechanical properties.^[1] Depending on the fabrication method, most of the hierarchically organized porous materials, which integrate various pore systems ranging from nano- to micro-regimes, have found promises for advanced performances in a wide array of technologies,^[2] comprising energy storage and conversion, catalysis, photocatalysis, adsorption, separation, sensing, and biomedicine.

Over the past decades, many processing techniques have been proposed to produce hierarchically organized porous materials. In these techniques, the 3D network formation mostly relies on the processing of the condensable molecular precursors through usually sol-gel route^[3] in the presence of soft^[4] and hard^[5] templates. In the soft templating approach, a surfactant in the sol-gel process of various molecular precursors is used to control the microstructure and pore size regime of the resulting material.^[4,6]

Dr. M.-A. Shahbazi^[†]
Department of Pharmaceutical Nanotechnology
School of Pharmacy
Zanjan University of Medical Sciences
Zanjan 45139-56184, Iran

 The ORCID identification number(s) for the author(s) of this article can be found under <https://doi.org/10.1002/adem.202000033>.

^[†]Present address: Drug Research Program, Division of Pharmaceutical Chemistry and Technology, Faculty of Pharmacy, University of Helsinki, Helsinki FI-00014, Finland

© 2020 The Authors. Published by WILEY-VCH Verlag GmbH & Co. KGaA, Weinheim. This is an open access article under the terms of the Creative Commons Attribution-NonCommercial-NoDerivs License, which permits use and distribution in any medium, provided the original work is properly cited, the use is non-commercial and no modifications or adaptations are made.

DOI: 10.1002/adem.202000033

Dr. M. Ghalkhani
Department of Chemistry
Faculty of Science
Shahid Rajaee Teacher Training University
Lavizan, P.O. Box 1678815811, Tehran, Iran

Dr. H. Maleki
Institute of Inorganic Chemistry
Department of Chemistry
University of Cologne
GreinstraÙe 6, Cologne 50939, Germany
E-mail: h.maleki@uni-koeln.de

This approach often results in materials with a dual mesoporous structure. In hard templating, the scarifying secondary phase, or porogen-like colloidal crystals are loaded into the main sol of the colloidal particles or molecular precursors before gelation/solidification, and then removed after the gelation process to create microstructures with organized multimodal porosity in the final structure.^[7] Removal of hard templates often requires harsh procedures, such as dissolution, chemical etching, or combustion methods, resulting in costly, tedious, and suboptimal approaches for mass production.^[3,8] Hüsing and coworkers^[3] have already reviewed all the techniques developed for the fabrication of hierarchically organized porous materials. In this Review, we limit to those anisotropic (e.g., biomimetic) architected porous materials that are exclusively processed through the so-called directional freeze-casting or ice templating approach. The freeze-casting synthesis approach, pioneered by Fukasawa et al.^[9] has drawn a significant deal of attention as a relatively cost-effective, versatile, fast, and green hard templating method to produce 3D structures with well-defined macroporosity. The general attempt is to indicate that the marriage of materials chemistry with ice physics can often lead to the fabrication of ultralight and superelastic cellular-based materials. In this approach, the directional thermal gradient results in in situ ice crystal nucleation and growth within the suspension and creates a temporary ice lamellar template. The growth of ice lamellar expels the particles/polymers/sheets in the slurry as they grow and confines them into the interstitial space between the ice (Figure 1).^[13] Therefore, a highly aligned and well-ordered continuous 3D open porous material is obtained after sublimation of the ice template, which is indeed a negative replica of the ice template.^[14] The monolithic body, resulted from thermally induced phase separation, can either be used as it is or sintered or calcinated, depending on the nature and characteristics of the materials and the final forethought products.

In directional freeze-casting, micrometer-sized ice crystal acts a dual role as both hard templates to develop macroporosity and also a self-assembly driver, leading to the rejection of the initially suspended slurry precursors or nanoparticles from the freezing front and their accumulation in the intercrystal spaces.^[13] The assembly of particles upon freezing is provoked through 1) a progressive increase in the particles' concentration in the intercrystal spaces upon shear force imparted by solvent removal, and 2) rotational movement of particles induced by the growth of the ice crystals. Final nondestructive removal of ice template under significantly mild conditions, usually via freeze-drying or sublimation approach, results in solid materials.^[15] Such benign template removal condition, alongside the fact that freeze-casting relies primarily on the physical phenomena, makes this approach amenable for the assembly of diverse array of complex structures from different building blocks, including ceramics,^[16] polymers,^[1c] carbons,^[17] and composites,^[18] using a wide range of primary solution, i.e., aqueous sols, hydrogels, polymer slurries, and 2D nanosheets.^[19]

The unidirectional freezing of the slurry triggers the ice crystallization and growth in a certain direction; therefore imposes assembling the macroscopic bodies with a spatially oriented macroporosity and anisotropic properties.^[20] Furthermore, this assembling technique gives the opportunity of not only developing 3D porous materials with sophisticated well-aligned



Mohammad-Ali Shahbazi received his Ph.D. in 2015 from University of Helsinki, Finland, where he worked on porous materials for drug delivery to cancer tissues. He is currently a postdoc scientist at Faculty of Pharmacy, University of Helsinki, working on therapeutic microdevices for autoimmune diseases. He is an expert in oral peptide delivery and fabrication of cell-mimicking carriers. His current research interest includes nano-based regenerative hydrogels for wound healing, bone repair, and long-term drug delivery.



Masoumeh Ghalkhani received her Ph.D. degree in 2010 from Sharif University of Technology (SUT) with specialization in the preparation and application of chemically modified electrodes. During 2009–2010, she was a visiting researcher at Department of Chemistry of the University of Coimbra, Coimbra, Portugal. She is currently acting as an

associate professor at Shahid Rajaee Teacher Training University, Tehran, Iran. Her current research and interest include synthesis of nanomaterials for several applications namely electroanalytical chemistry, electrocatalysts for fuel cells, batteries, and biosensors.



Hajar Maleki received her Ph.D. degree in 2014 from University of Coimbra, Portugal, with a focus on development of hybrid aerogels for energy saving applications. She is currently acting as a Habilitand at Institute of Inorganic Chemistry of University of Cologne, Germany. Her current research focuses on fabrication of 3D nanostructured

porous materials with mechanical flexibility, directed shape morphosis, and controlled microarchitecture using bioinspired fabrication techniques of 3D printing and freeze-casting for different applications namely for bone repair, thermal insulation, and environmental applications. She is also the recipient of several prestigious national and international grants.

microarchitecture namely lamellar, honeycomb, and nacre-inspired brick-and-mortar (Figure 1),^[10] but also the 2D oriented surface patterns^[1c] and recently is extended to the micrometric spheres or beads.^[1c] As the process does not require any chemical reaction, any potential complications associated with byproduct removal or purification procedure is also avoided.^[10b]

Based on the recent advancement in freeze-casting methods, this templating approach is also extended for mimicking the structures found in natural materials to create bioinspired porous composites with the capability of controlling the hierarchical

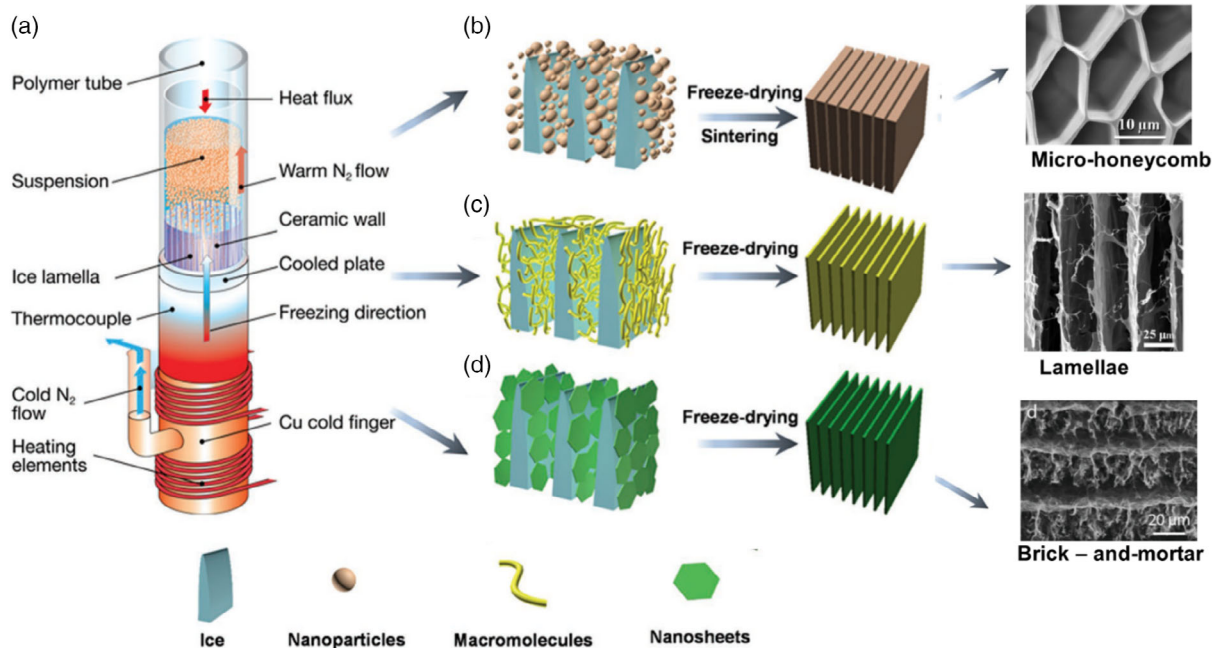


Figure 1. a) Schematic of the freeze-casting technique to prepare bioinspired nanocomposites. As the ice grows, it expels the b) nanoparticles, c) macromolecules, and d) nanosheets that accumulate in the space between ice crystals. The micro-honeycomb, lamellar, and nacre-mimetic brick-and-mortar structure, where the pores are a direct replica of the ice crystals, were obtained. After sublimating the water (or another solvent), ceramic, or metal scaffolds were thermally treated to sinter and consolidate the structure. Reproduced with permission.^[10a,11a,12] Copyright 2014, 2017, and 2004, Nature Publishing Group, Wiley, and Royal Society of Chemistry, respectively.

structure and mechanical toughness.^[10a,11] The directionally freeze-casting materials have found breakthrough applications in the various fields, including structural biology,^[11b,21] thermal insulation,^[22] environmental application,^[23] pressure sensor,^[24] and energy storage and conversion,^[25] among others. The lightweight, mechanically strong, highly ordered nanohybrid foams with cellular structures have been used as thermally superinsulation materials with an anisotropic heat conduction behavior with the purpose of thermal energy management.^[26] Furthermore, flexible foams made of electrically conductive carbonaceous materials or electrically conductive polymers have been used as a soft and flexible pressure sensor as well as in soft electronic systems.^[24a,27] This synthesis approach can also be extended for obtaining compressive cellular materials with the capability of pollutant absorption from the liquid and gas phases.^[28] In this regard, due to the enhanced capillary flow of liquids/pollutants in the aerogel channels, the absorbability and recyclability of the anisotropic aerogels have drastically been increased. In tissue engineering, for example, anisotropic 3D porous systems of aligned nano- and microstructures are believed to be important in guiding cell growth or tissue regeneration, resembling the function of anisotropic porous native extracellular matrix (ECM).^[29]

In this Review, the aim is to give a brief overview of the recent advances in developing anisotropic porous inorganic, organic, hybrid, and carbonaceous materials with a special emphasis on materials with biomimicking microstructure using directional ice templating approach. The priority is given to the materials that have been exclusively developed in an aqueous

system, e.g., using water as a dispersing medium and to highlight their applications in various advanced technologies.

2. Ice Growth Mechanism and Orientation of Macroporosity

Understanding and controlling the growth of ice crystals is of interest in the development of desired pore morphology. The microarchitecture, physical, and mechanical properties of ice templated materials are extremely controlled by the morphology and direction of the ice crystals. The shape and dimension of the ice crystal grown during freezing can be governed by the cooling rate, the temperature gradient, the concentration and the composition of slurries, solvent type, the pH condition, or sometimes the presence of the externally applied magnetic or electric field. In addition, the presence of tensoactive additives with facet sensitive adsorption properties^[9] like sucrose, alcohol, or addition of some polymers like poly(vinyl alcohol) (PVA)^[30] and polyethylene glycol^[31] in slurries has also shown to regulate the viscosity, surface tension, freezing point of slurries, and consequently, the growth kinetics, behavior, and direction of the ice crystals. The variation in the ice growth pattern can eventually define the final characteristics of the pores and overall microstructure morphology in the freeze-cast materials.^[19,32] In addition, the solvent also plays a major role in the microstructural pattern of the final product.^[11b] Four commonly used solvents in freeze-casting are water, camphene, camphor-naphthalene,

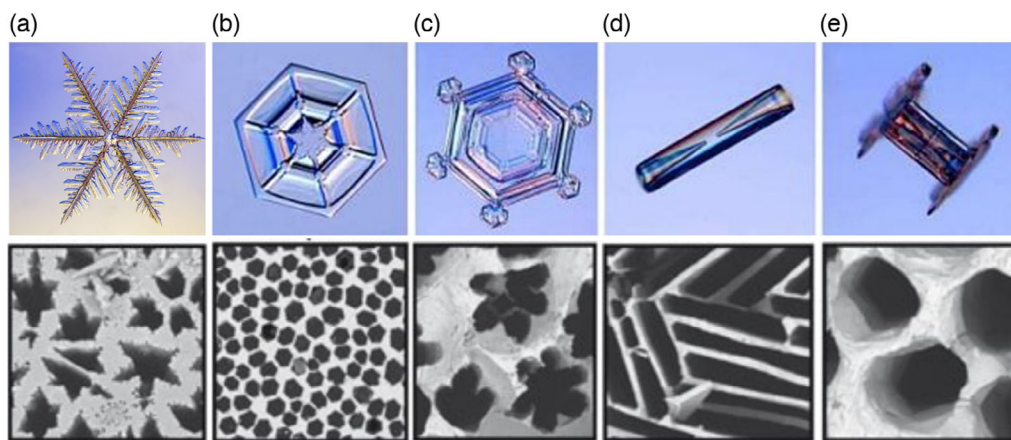


Figure 2. Different ice crystals grown in various temperatures and humidity in vapor phase, and typical pore shapes obtained by ice-templating in liquid phase, including a) dendrite, b) plate, c) sectored plate, d) needle, and e) hollow column. Reproduced with permission.^[15,34a] Copyright 2014 and 2017, Materials Research Society, respectively.

and *tert*-butyl alcohol, each creating a particular pore architecture, including lamellar, cellular, dendritic, and prismatic, respectively.^[16]

According to Gibbs–Curie–Wulff Theorem,^[33] the ice crystals grow in a variety of symmetrical morphology of snow flakes: dendritic (snowflakes), plates, needles, hollow columns (fingerlike), or smoothed plates or faceted structures in the vapor phase.^[34] However, extremely depending on the supersaturation of water in the surrounding environment (Figure 2), these growth mechanisms cannot be reproduced in a straightforward approach in a liquid phase. Nevertheless, nearly the same snow-flake morphology is generated in the liquid phase in the ice-templated materials (Figure 2).^[34a] The growth behavior of the ice crystal during ice templating is not fully understood. However, it seems to be largely controlled by a combination of phenomena, including molecular attachment kinetics on faceted surfaces and large-scale diffusion processes at the ice crystal surface.^[34a] Several approaches have been proposed to follow the growth mechanism of ice crystals and behavior of the slurry particles in situ, including time-lapse computed X-ray tomography,^[35] time-lapse in situ confocal microscopy,^[36] and transmission electron microscopy,^[37] among others. But none of them yet provided the 3D real-time observations without influencing the system.

The direction of solidifications can govern the orientation of the macropore channel. In the majority of the ice templating process, the mold in which the slurry is initially cast is usually left in contact with a cold surface at a certain time. The ice grows along the imposed thermal gradient, for example, vertically from the bottom of the mold when the bottom of the mold is unidirectionally cooled to create the anisotropic macropore channels. One example in this regard is the work of Zhang et al.,^[38] who prepared long-range vertically aligned graphene sheet membranes (VA-GSMs) as the highly efficient solar thermal converter for the generation of clean water. In their work, graphene oxide (GO) suspension was mediated with a certain amount of ethanol and then transferred to a polytetrafluoroethylene (PTFE) mold, which was placed on the surface of liquid nitrogen for freeze-

casting. With precise control on the freezing direction from bottom to top, a 3D graphene membrane with the vertically aligned assembly of graphene sheets was obtained (Figure 3i). In this particular study, ethanol was specifically used as the antifreeze agent to decrease the freezing point and, therefore, to tune the crystallization behavior of the ice growth, resulting well-aligned assembly of graphene in the direction of ice crystal axes. However, ice can also grow in different orientations depending on the imposed thermal gradient during the freeze-casting.^[16] In a study by Moon et al.,^[40] ice was grown radially from the inner part of the metallic cylindrical mold to the center of the slurry where a Teflon rod was placed. The final tubular structure exhibited radially oriented pore extending from inside toward the outside of the tube.

Bidirectional freeze-casting is also another recently proposed technique reported by Bai et al.^[41] to fabricate long-range ordered (centimeter scale) 3D structures with a high level of control over hierarchical architectures. The bidirectional freeze-casting is basically known as a kind of potent bioinspired fabrication technique that can develop and design the sophisticated hierarchical structures ranging from nano-/micro- to macroscopic levels with a remarkable mechanical strength similar to that of many natural porous materials. In this regard, a nacre-mimetic composite of hydroxyapatite/poly(methyl methacrylate) (PMMA) with brick-and-mortar pore morphology has been created by bidirectional freezing.^[41b] Yang et al.^[39] have used this technique to achieve a multiscale, highly porous architecture, and mechanical robustness simultaneously. Inspired by *Thalia dealbata* stem, this group applied a bidirectional freezing technique and assembled GO sheets to a biomimetic-architected 3D aerogel (Figure 3ii). This was conducted by introducing polydimethylsiloxane (PDMS) wedge with a slope angle of around 15° between the cooling stage and precursor suspension, which could generate dual temperature gradients (both horizontal [ΔT_H] and vertical [ΔT_V]) during freezing. Ice growth and direction and therefore final microarchitecture in freeze-cast materials, such as porosity and its orientation were regulated by various parameters,

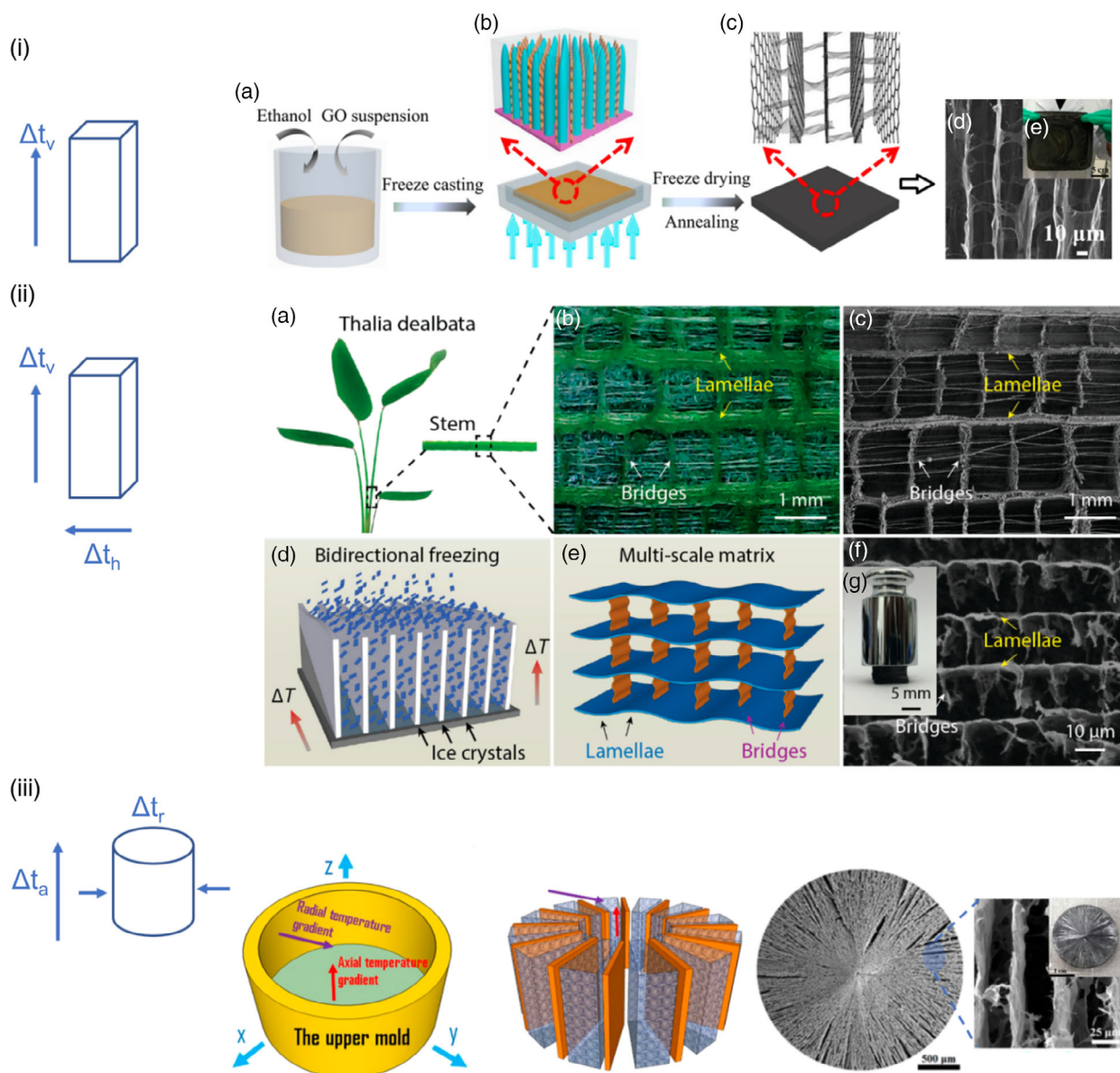


Figure 3. i) Schematic of the fabrication process of VA-GSM. a) GO suspension with a small amount of ethanol. b) Directional freeze-casting of GO mixture in a PTFE mold, which is placed on the surface of liquid nitrogen to induce the freezing direction from the bottom to top. c) VA-GSM is obtained after freeze-drying and thermal annealing. d) SEM images of VA-GSM with different magnifications. e) Photograph of monolith VA-GSM with a size of 16 cm × 16 cm. Reproduced with permission.^[38] Copyright 2017, American Chemical Society. ii) Architecture of the *T. dealbata* stem and biomimetic graphene aerogel. a) Optical image of a *T. dealbata* stem. b, c) Optical and SEM images showing the multiscale architecture, where oriented lamellar layers (thickness: ≈100 μm) are connected by interlayer bridges (length: ≈1 mm). d) In a bidirectional freezing technique, a low thermal conductive wedge was first placed between the GO/PVA suspension and cooling stage. When freezing, it simultaneously generated horizontal (ΔT_H) and vertical (ΔT_V) temperature gradients. e) The schematic of the as-prepared graphene aerogel with plant stem-like architecture. f) SEM image showing the detailed architecture of the biomimetic graphene aerogel, where lamellae are connected by interlayer bridges, observing from the cross-section parallel to the cooling stage after bidirectional freezing and thermal reduction. g) Optical images showing a cubic aerogel sample (10 × 10 × 10 mm³) which supports >6000 times of its own weight with around 50% strain. Reproduced with permission.^[39] Copyright 2017, Nature Publishing Group. iii) Illustration of a radiating GO and GO/cellulose nanofiber (CeNF) nanocomposite aerogel with an obvious radiating pattern on its surface aerogel fabricated by bidirectional freezing using a copper mold. SEM images showing details of the channels in the marked region. Reproduced with permission.^[17] Copyright 2018, American Chemical Society.

including concentration and viscosity of the suspension, the slope angle of PDMS wedge, cooling rate.^[41a] The developed aerogel had an architecture with lamellar layers intercon-

nected by bridges, whereas it was concurrently strong, flexible, and lightweight similar to what observed in *T. dealbata* stem.

As another example of bidirectional freeze-cast material, Wang et al.^[17] developed GO aerogels with a trend of centrosymmetric assembling of the GO sheets into a vertical and radially aligned structure with centimeter-length scale domains. This was achieved via controlling the ice growth direction by casting the initial slurries inside a copper mold, providing cooling source radially (*r*) and axially (*a*) (Figure 3iii) but also in the presence of some ice crystal shape controlling additives/agents like chitosan, cellulose, and ethanol. The bidirectional freezing imposed two perpendicular temperature gradients into the slurry, leading freeze-cast GO to assemble in a spiral pattern with pore channel size increase with distance from the center.^[17,42]

3. Directional Freeze-Casting for the Development of 3D Functional Structures

The directional ice templating approach is proposed as an environmentally friendly, straight forward, and reproducible technique for the development/shaping of various materials, namely ceramics, polymers, different carbonaceous materials, e.g., GO, carbon nanotube, and their composite with unique topological microarchitecture. In this section, we have highlighted the use of this technique for the processing of materials mentioned earlier, with particular emphasis on the most updated works in the literature for the development of porous 3D monoliths' structures. A very brief overview is also provided for using the directional freeze-casting approach for the formation of micrometer-sized particles/porous beads, fibers, and films.

3.1. 3D Monoliths

3.1.1. Ceramics

Ceramic cryogels/foams were first reported by Mahler and Bechtold,^[43] through freeze-drying of metal and metal oxide powders.^[44] Since then, numerous works have been reported^[45] for the preparation of various ceramic-based 3D materials, such as alumina, silica, titania, hydroxyapatite silicon oxycarbide, to name only a few. Mukai et al.^[12] used pseudo-steady-state unidirectional freeze-casting (UFC) method on the freshly gelled silica hydrogel and developed monolithic silica aerogels (after freeze-drying) which have an array of flawless micro-honeycomb-like macropores which whose wall were micro- and mesoporous (Figure 4i,a,b). In another study by the same group,^[48] the size of the micro-honeycomb pores, as well as their wall thickness, were systematically controlled by freezing rate through changing the immersion rate of gel into a cold bath, as well as changing the freezing temperature without varying the micro-/mesoporosity of the honeycomb walls. At low immersion rate and low freezing temperature, the size of micro-honeycomb was quite larger than those that were developed in inverse conditions. However, the wall thickness as well as micro and mesoporosity in the wall of micro-honeycombs, greatly varied with pH and the concentration of initial SiO₂ sol. The cell size of micro-honeycombs structures ranged between 10 and 15 μm with micro- and mesoporosities (the Brunauer–Emmett–Teller [BET] surface area between 400 and 700 m² g⁻¹), which were originated from the voids between silica colloidal nanoparticles upon sol–gel reaction. Tamon and

coworkers^[49] developed ice-templated SiO₂–Al₂O₃ with almost the same micro-honeycomb structure with the macropore sizes of 10–20 μm and the wall thickness of 200–500 nm. Al atoms were incorporated into the silica network by the creation of an Al–O–Si polymeric network with a BET surface area of >700 m² g⁻¹.

Boron nitride nanosheets (BNNs),^[50] also known as white graphene, consist of hexagonal boron nitride (hBN) planes with multitude of interesting properties, such as wide energy bandgap, excellent oxidation resistance, electrical insulating property, and high thermal conductivity, have been proposed for wide range of applications mainly electronic devices and thermal energy management to name only few. However, in analogy with GO, to fully perceive BNNs' outstanding properties, it is very important to avoid agglomeration of BNN planes upon π-stacking interactions. One of the strategies to resolve the agglomeration issue is to process the BNNs as a 3D porous structure. Despite the sophisticated and cumbersome procedure that require explosive and hazardous precursors with extremely high temperature, anisotropic freeze-casting fabrication technique has been known as a relatively facile and green technique to process BN aerogels.^[26d,46] In majority of these studies, the self-assembled BNNs foams/aerogels showed density as low as 15 kg m⁻³, high porosity (99.3%), great resilience, and excellent hydrophobic nature.

In a recent work by Zeng et al.,^[46c] BNNs aerogels have been developed via polymer-assisted cross-linking and freeze-casting strategies (Figure 4ii). For polymer cross-linking, sodium cholate has been used first to functionalize the BNNs due to its strong affinity to the basal plane of BNNs through van der Waals interaction and hydrogen bonding, which was followed by cross-linking through the addition of butanediol diglycidyl ether (BDGE) via a ring-opening mechanism. The developed BNNs hydrogels were freeze-cast in an ice bath (–50°) followed by freeze-drying. The obtained aerogels comprised controllable well-ordered microstructures with reversible high compressibility up to 80% of strain. The anisotropic microstructure also resulted in anisotropic compressive behavior—being in-plane compression stress much lower than out-of-plane deformation.^[46c] The resulted BNNs possessed a high porosity, as high as ≈99%, with cell or pore size of ≈100 μm and the microstructural and pore morphologies aligned in the direction of ice growth. Most of developed BNNs aerogels were organized in a honeycomb-like morphology to enhance the elastic modulus and strength. At a lower scale, the pore wall comprised multilayers of face-to-face oriented BNNs cross-linked by the BDGE which interlocked with each other and led to the 3D network with high mechanical resilience.

It is quite challenging for materials scientists to realize highly mechanical resilient and elastic aerogels out of solely ceramic-based starting components. To this aim, Si et al.^[47] have developed scalable super elastic lamellar-structured fire resistance ceramic nanofibrous aerogels (CNFAs) from combining the strong and viscoelastic sol–gel-based electrospun SiO₂ nanofibers (206 nm) and aluminoborosilicates (AlBSi) matrices through the freeze-casting technique with controllable assembly (Figure 4iii,a–e). The electrospun randomly oriented flexible SiO₂ nanofibers were homogenized with aqueous polyacrylamide solution to wrap the fiber surface with a cationic charge to develop a well-dispersed solution upon mutual repulsion of charged fibers. The resulting stable solution was mixed with

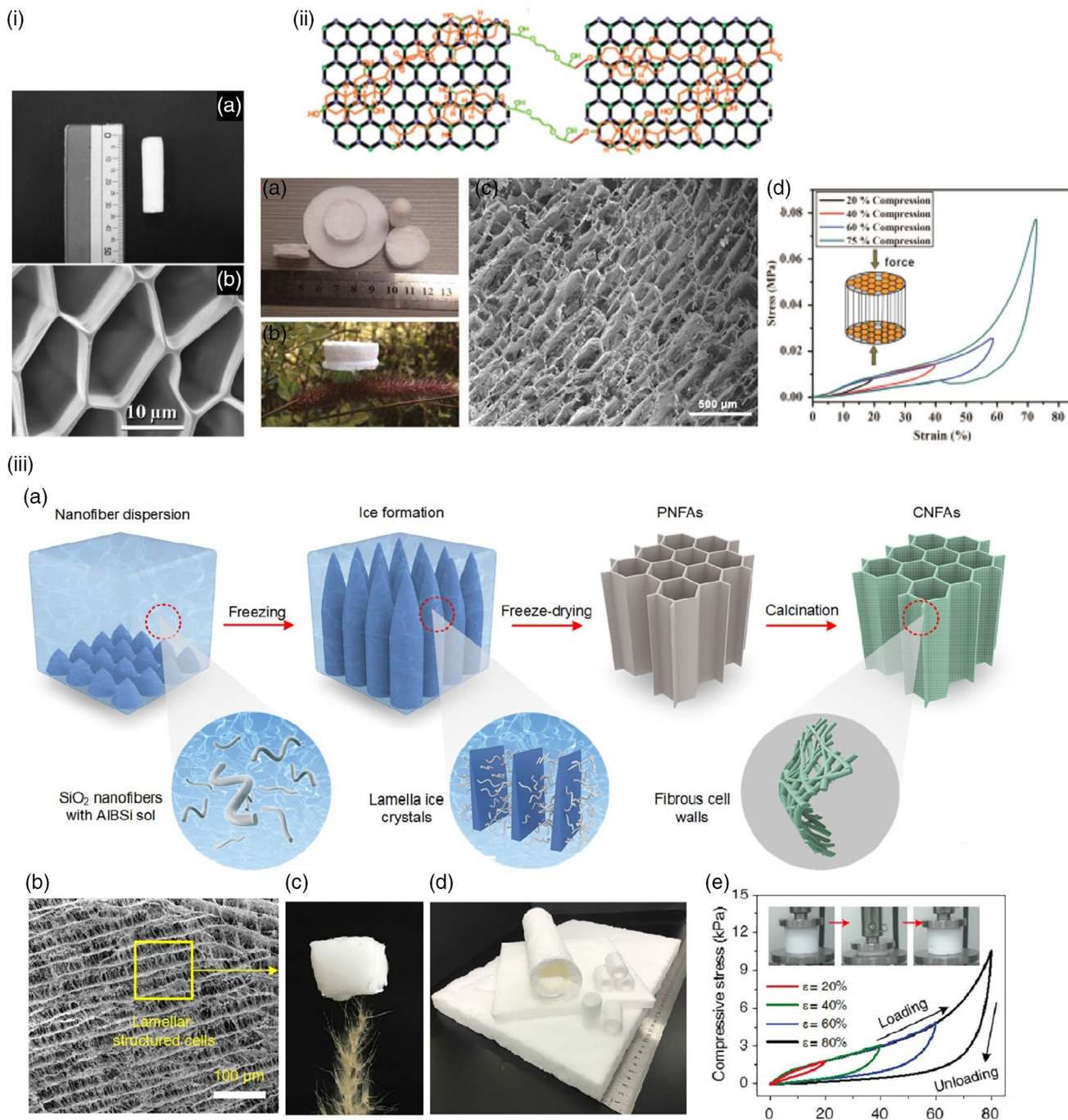


Figure 4. i) Macroscopic image of freeze-cast silica aerogel (a) with an SEM image indicating micro-honeycomb cross-sectional micromorphology (b). Reproduced with permission.^[12] Copyright 2004, Royal Society of Chemistry. ii) Macroscopic image showing the mechanism of formation of lightweight BNNs aerogels through cross-linking and anisotropic freeze-casting as well as their superelastic characteristics upon compression. Reproduced with permission.^[46c] Copyright 2015, American Chemical Society. iii) Schematic illustration of the fabrication of CNFAs (a). The microscopic structure of CNFAs demonstrates the hierarchical nanofibrous cellular architecture (b), an optical image indicating ultralightness (c), scalability of CNFAs (d), and compressive stress versus strain (e) curves during loading–unloading cycles with increasing ϵ amplitude. Reproduced with permission.^[47] Copyright 2018, AAAS.

AlBSi sol and frozen in a dry ice/acetone mixture, freeze-dried, and finally calcined at 900 °C. Cross-linking with AlBSi matrices formed robust silicate bonding between SiO₂ ceramic fibers and therefore increased the strength of the overall network. The final

ceramic aerogels exhibited ultralow density (0.15 kg m⁻³) recoverable elasticity even at a high temperature (e.g., 1100 °C) due to the evolution of crystalline β -quartz phase in the silica fibers with a hierarchical cellular nanofibrous architecture.

3.1.2. Carbon

Thanks to its superb properties, such as large specific surface area, lightweight, high porosity, chemical inertness, and good conductivity, carbon aerogels have largely aroused the attention in many fields, such as flexible conductors, electrode materials for energy conversion and storage, sensors, catalyst support, and absorbent.^[51] Multifunctional carbon aerogels have been developed from various starting raw materials, such as biomass-derived aerogels (i.e., chitosan, catkins, bacterial cellulose, bamboo, sugar cane, cotton, etc.),^[52] carbon nanotube-based aerogels,^[51b] graphene, and graphene/(bio)polymer-based aerogels and so on.^[53]

Among the starting precursors listed earlier, GO aerogel is one of the most attention-getting carbon-based aerogels with very good physical and mechanical properties. Processing the GO into aerogel, for the first time by Wang et al.,^[54] has become an important archetype as it led to the successful marriage of outstanding intrinsic properties of graphene with exciting aerogel properties. GO aerogels are usually prepared by a sol-gel process where the 3D interconnected GO is initially formed via gelation of GO dispersion by adding cross-linkers, reducing agent, or treating at an elevated temperature and pressure using a hydrothermal method, followed by supercritical or freezing drying technique.^[55] In most of the cases, the sol-gel process gives rise to ultralow density, high porosity, high electrical conductivity, and excellent compressibility. But the preferred anisotropic orientation of the nano- and microstructure originated from directional self-assembly of GO nanosheet along a certain direction during the process has not met with this approach, and the final aerogels have a randomly oriented porous microstructure. Porous GO structure developed by different techniques, including chemical vapor deposition (CVD),^[56] cross-linking self-assembly, and self-assembling at high pressure and temperature

followed by freeze-drying failed to show ultralow density due to the inevitable stacking of the GO sheets during the self-assembly process.^[57] A template-dependent technique like, for example, deposition of GO solution on nickel foam^[58] could produce the light and highly porous GO sponges, but this technique also suffered from high cost, low yields, and template residue after etching.^[59] Directional freeze-casting has been known as a very effective technique for integrating and self-assembling the GO sheets into the 3D interconnected macroscopic aerogels structure.^[57,60] A controllable and scalable assembly of the GO sheets through a wet shaping technique of UFC has resulted in superlight and mechanical resilient GO aerogels with microstructures that were aligned in the ice growth direction.^[27b,54,57,59]

Modern structural analysis techniques have indicated a lot of biological examples in nature with cellular and lightweight structure yet mechanically strong and resilient.^[61] One striking example in this regard is cork which its efficient hierarchical structural assembly is a key for its lightweight and high specific mechanical strength and elasticity. The cellulose nanofibers in the cork's cell walls are tightly packed in an ordered manner to increase the strength.^[61] Then the honeycomb-like microstructure, which is known as a geometry to maximize bulk-specific elastic modulus in the cork and wood, are formed by connecting the individual cells with a dimension of tens of micrometers. In this regard, cork-mimetic graphene monoliths with honeycomb cellular microstructure^[62] were fabricated by freeze-casting of a partially reduced (r) GO solution (Figure 5a) without any need to the additional polymer binders, freeze-drying, and annealing at 200 °C. The resulting biomimetic graphene-based monoliths exhibited a combination of controllable ultralow density ($\approx 0.5 \text{ kg m}^{-3}$), high porosity (99.9%), and superelasticity.

As it is evident from scanning electron microscopy (SEM) and high-resolution transmission electron microscopy (HRTEM)

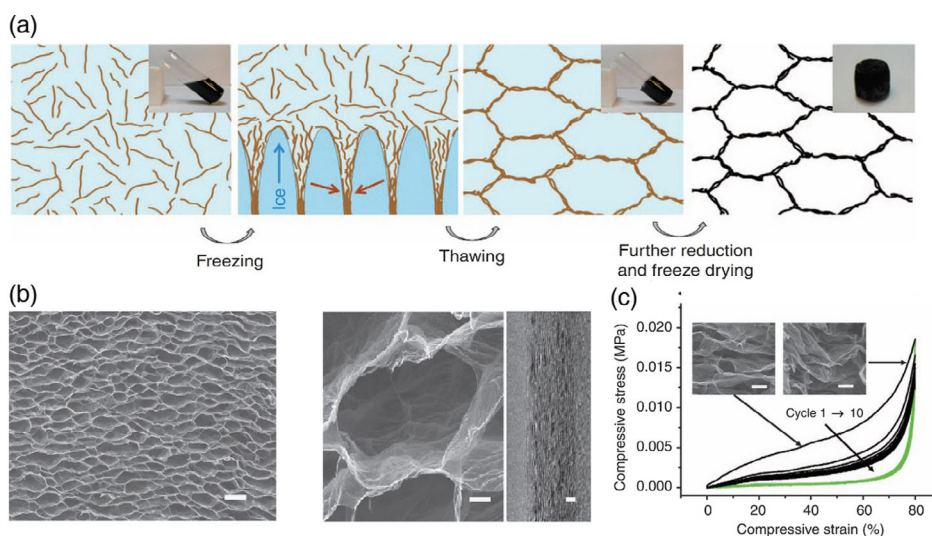


Figure 5. a) The scheme shows the formation mechanism of the cork-like elastomer monolith by freeze-casting. When a well-dispersed GO dispersion (the first scheme) is frozen, GO sheets are concentrated at the boundary of ice crystals and then aligned along the growth direction of ice due to the squeezing effect. As a result, a continuous honeycomb-like network is formed. The network retains its connectivity when the ice is thawed. b) SEM and HRTEM images of graphene monolith of 5.10 kg m^{-3} . Scale bars are 50 and 10 μm in SEM images and 2 nm in TEM images. c) Compressive stress-strain curves of 10 cycles of loading (black lines) and unloading (green lines). The insets show the SEM images of the elastomer under compression at different strains. Scale bars 10 μm . Reproduced with permission.^[62] Copyright 2012, Nature Publishing Group.

analyses (Figure 5b), freezing has simultaneously induced the GO sheets in each cell wall to be oriented in a highly ordered fashion, mimicking both micro- and nanometer-scale structure found in the cork. The honeycomb-like cellular structure possesses the cell dimension in the order of tens of micrometers and the cell walls' thickness of ≈ 100 times thinner than that of the cork (≈ 1 mm). This highly ordered cellular microstructure rendered the graphene monolith to compress to at least 80% of strain and almost entirely recovered to its original shape when the loading was removed (Figure 5c).

Chen et al.^[63] developed scalable carbon aerogels by inspiring from the structure of the hierarchical lamellae-bridge structure of *T. dealbata* plant stems and managed to fabricate an ultralight, superelastic, highly conductive anisotropic carbon aerogel from an assembly of konjac glucomannan (KGA) with GO precursors using bidirectional freeze-casting approach (Figure 6a). The unique layered structure of KGA/GO aerogels not only enabled the final carbon aerogel with a low density of 4.2 kg m^{-3} , high elasticity up to 80% of strain and over 1000 strain recyclability, but also endowed a high electrical conductivity (12.9 S m^{-1}) to final aerogels with high potential application as piezoresistive sensors and supercapacitor electrodes (Figure 6b–e). It has been shown that the freezing temperature could play an important role in determining the porous structure: for example, casting at -196°C produced GO aerogels with small cellular pores ($10 \mu\text{m}$) and thin pore walls (20 nm), whereas freezing at -10°C resulted in GO aerogels with larger lamellar pores ($800 \mu\text{m}$) and thicker pore walls ($80 \mu\text{m}$).^[64] In addition, the concentration of the initial GO solution together with the size of GO precursors has also shown to influence the pore size as well as mechanical, physical, optical, and transport properties of GO assemblies.^[27b,65]

3.1.3. Polymers and Hybrids

Directional freeze-casting is also known as a promising method for the fabrication of anisotropic, polymeric cryogels/aerogels with a well-defined pore structure. In this method, usually, precursor solutions or suspensions of monomers or polymers are frozen under a unidirectional temperature gradient, which has been used to develop anisotropic hydrogels or aerogels with sophisticated structure and morphologies.^[66]

In general, to fabricate porous polymeric monoliths by the freeze-casting approach, a polymer is dissolved in an appropriate solvent, and the resulting solution is then frozen and freeze-dried. Alternatively, one can also consider to dissolve monomers in a solvent, freeze the resulting solution, and polymerize the monomers in the frozen state.^[67] The solvent can be removed by freeze-drying or under vacuum at ambient temperature. Cryopolymerization^[68] is a technique where a monomer solution in a frozen or semifrozen state is polymerized at subzero temperature to produce macroporous gels. With a combination of cryopolymerization and directional freezing, aligned porous hydrogels from poly(ethylene glycol),^[69] which was polymerized in the freezer at -15°C for 12 h as well as urethane diacrylate-dioxane system (ultraviolet [UV] polymerization)^[66a] have been prepared. Barrow and Zhang^[67] have produced cross-linked aligned porous materials by directional freezing and UV frozen polymerization of dimethacrylate monomers with various organic solvents. In general, to inhibit the redissolution or hydrolyzing the freeze-cast gel, upon immersion in water, postprocessing of the gel through photocross-linking or photopolymerization was conducted.^[69] These materials exhibited enhanced mechanical stability with the aligned porous structure used as a stationary phase for high-performance liquid chromatography, showing

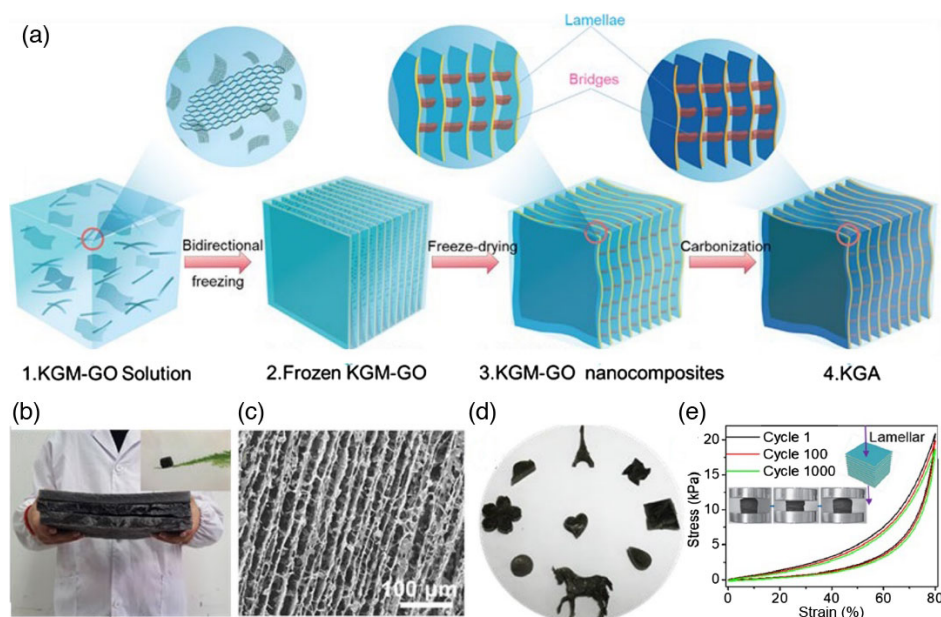


Figure 6. Preparation and morphology characterization of *T. dealbata* inspired anisotropic cellular biomass-derived carbonaceous aerogel. a) Schematic illustration of the manufacture of KGAs. b) Photograph of a large-scale KGA-3 (the inset shows KGA-3 standing on the tip of *T. dealbata*). c) SEM images of 3D mineral bridge structure of KGA-3. d) Digital photo of KGA-3 with various shapes. e) Compressive elasticity (stress–strain curves) of lamellar KGA-3 at 80% strain for the first 1000 cycles. Reproduced with permission.^[63] Copyright 2018, American Chemical Society.

fast mass transfer kinetics with low backpressure. Thanks to the high material compatibility with the directional freeze-casting process, this process is amenable to synthesize not only single-component materials but also hybrid structures.^[22b,29a,70] Therefore, this enables a wide spectra of properties using synergisms between various structural components, such as ceramic/polymer bodies combining high fracture toughness with high ductility or lightweight, and electrically conductive graphene/polymer composites and so on. Wang et al.^[54] developed super-light GO/epoxy composite aerogels with a directional freeze-casting approach and obtained aerogels with the orientation of GO sheet in a preferred direction with exceptional anisotropic structure and properties.^[71] The assembly of GO in a certain direction led to significant anisotropic electrical conductivities in GO aerogels, promising for many important applications.^[59] Novel BNNs/epoxy composite aerogels have been obtained with controlled anisotropic freeze-casting, leading to 3D BNNs

network into the epoxy resins to obtain novel polymeric composite aerogels for high thermal conductivity applications.^[72]

Chau et al.^[29b] developed structurally and mechanically anisotropic composite aerogels and hydrogels composed of aldehyde-modified cellulose nanocrystal (A-CNCs) and hydrazide-functionalized poly(oligo ethylene glycol methacrylate) (POEGMA) through simultaneous freeze-casting and cross-linking processes (Figure 7i). Chemical cross-linking through the formation of hydrazone between components was vitally important for structural integrity and stability of the aerogel/hydrogel in water as well as for final biomedical applications. The microstructure of the resulting hydrogel/aerogels was controlled by varying the weight ratio of the CNC to POEGMA, the total concentration of these components and freeze-casting temperature. The general trend for the structural changes in developed gels is shown in Figure 7ii, which was designated as the fibrillar (F), columnar (C), and lamellar (L)

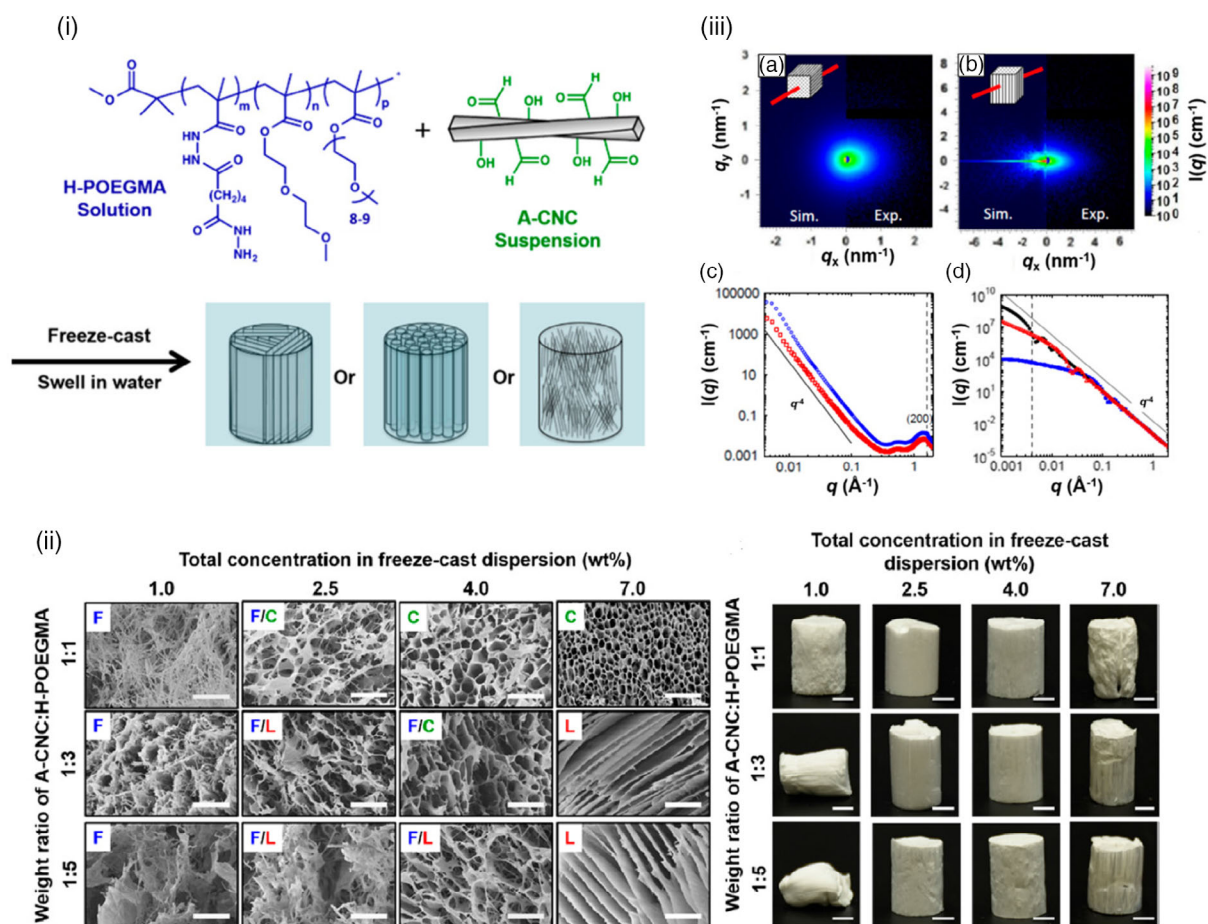


Figure 7. i) Cross-linking reaction of A-CNCs with hydrazide-functionalized POEGMA (HPOEGMA) and illustration of morphologies of hydrogels achieved via the freeze-casting process. ii) Left: SEM images of aerogels cross-section (the XY-plane perpendicular to the ice-growth direction) with morphologies ranging from fibrillar (F) to columnar (C) to lamellar (L) and their combinations, dependent on A-CNC/H-POEGMA weight ratio and $C_{A-CNC+H-POEGMA}$. Scale bars are 20 μm . Right: Photographs of aerogels cast in cylindrical molds. Scale bars are 0.5 cm. iii,a) Experimental 2D SAXS pattern from irradiating the 1:5-4 aerogel in the Z-direction. iii,b) Experimental 2D SAXS pattern from irradiating the 1:5-4 aerogel in the XY-direction. iii,c) 1D radial-averaged SAXS plots of the 1:5-4 aerogel irradiated in the Z-direction (blue) and XY-direction (red). A line with q^{-4} scaling is also shown as a visual aid. iii-d) Theoretical 1D radial-averaged SAXS plots for small cylinders (blue squares) with a radius of 3 nm ($\pm 10\%$) and a length of 150 nm; large cylinders (red triangles) with a radius of 65 nm ($\pm 10\%$) and a length of 50 μm ; discs (black dots) with a radius of 5 μm and a diameter of 260 nm ($\pm 10\%$). The dotted line marks the lower limit of the experimentally reachable q range. Reproduced with permission.^[29b] Copyright 2016, American Chemical Society.

structures. For example, at a high total concentration of precursors ($C_{A-CNC+HPOEGMA}$) and a low weight fraction of A-CNCs, the aerogels had a lamellar morphology with ≈ 200 nm-thick and an interlamellar distance of $7 \mu\text{m}$. In addition, the freezing temperature and the rate of ice crystal growth in the sample have greatly controlled the aerogel morphology. The aerogel freeze-cast at -20°C created a more well-defined lamellar-like structure than the same sample prepared at -80°C . Small-angle X-ray scattering (SAXS) was used to provide insight into the average volume structure of developed aerogels. As it is evident from the SAXS data and theoretical simulation of 2D SAXS pattern, irradiation in XY-direction yielded the anisotropic (ellipsoidal) 2D pattern, whereas in Z-direction, the 2D pattern was isotropic (circular) (Figure 7iii). These results implied that scattering objects or mesostructures (with a size >100 nm) were aligned in the Z-direction but not within XY-plane. In addition to the anisotropic behavior in the microstructure, aerogels have also indicated a direction-dependent Young's moduli, which could be interesting for mimicking biological tissues.

3.2. Films

In most of the studies, which are hitherto reported, the directional freeze-casting technique has been utilized with the purpose of the development of truly 3D porous materials in the monolithic forms with a microstructural complexity. However, Estevez et al.^[73] developed an electrically conductive, macroporous hybrid film with 3D open porous network structure from graphene nanosheets (GS)-supported platinum (Pt) nanoparticles, which were well dispersed in an ionomer (Nafion). The film has been developed using a simple approach of dip-coating the substrate (of any type) inside the aforementioned mixture followed by freeze-casting the developed film and subsequent reduction of the graphene. With this technique, a multifunctional film with a thickness of a few millimeters has been obtained. The developed film could combine electrical (graphene) and ionic conductivity (Nafion) and catalytic activity by

Pt as well as high porosity which is developed due to the cryoprocessing. Due to the ice templating, the film samples show lamella arrays, which were perpendicular to the film surface. In the developed film, in addition to the macroporosity triggered by cryocasting, Nafion also contains inherent nanoscale porosity arising from the clustering of its ionic domains.^[74] Therefore, the induced nano- and macroporosity in the developed multi-component Nafion/GS/Pt film, together with its interesting physicochemical and mechanical resilience originated from its cellular microstructure, made the film interesting for several important technological applications ranging from the sensor to membrane electrode assemblies in fuel cells.^[73]

To develop GO supercapacitor films with a high-power density and a short charging time, it is very important to prevent the π - π stacking between graphene sheets. This can be obtained through the processing of the GO film with an open hierarchical porous structure. Among the existing method, Shao et al.^[75] fabricated 3D hierarchical porous graphene films by filtration assembly of partially reduced (rGO) microgel and a subsequent freeze-casting technique (Figure 8a-d). The ice crystals were grown between the prerduced GO sheet microgel with a 9% volume expansion. The morphology of the solidified ice crystals governed the porous characteristic of the final GO film. Herein, to prevent the high extent of aggregation of GO sheets during assembly and provide enough space for ice crystal growth within the gel network, the prerduction of GO sheets prior to filtration and freeze-casting was conducted. The resulting porous graphene films exhibited a combination of useful properties, including good electrical conductivity, high mechanical strength, and extremely high performance in supercapacitors.

3.3. Fibers

Many applications of electrospun fiber can be highly extended when the surface area and porosity in fiber are increased. For this, many reliable fabrication techniques have been so far proposed by several groups.^[76] These methods usually relied on

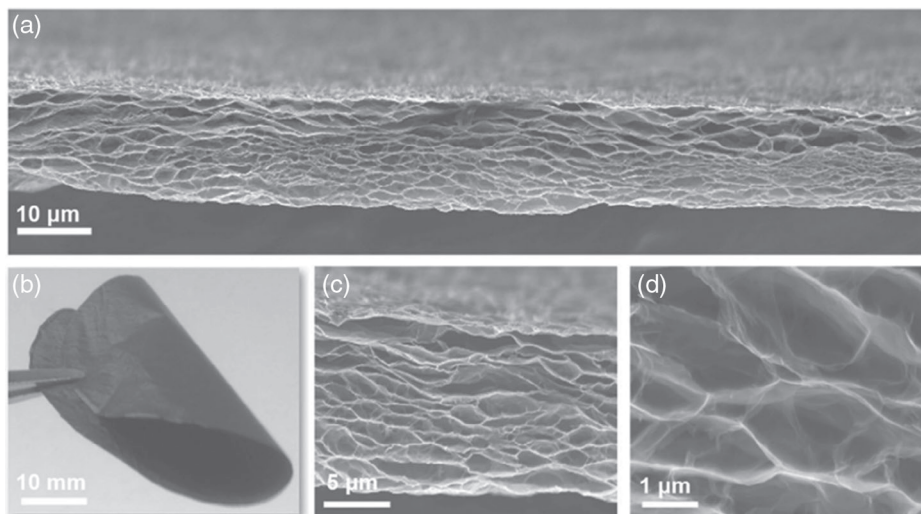


Figure 8. Morphology of 3D porous rGO films. a) Cross-sectional SEM image of a 3D porous rGO film after long-term reduction. b) Photograph of a bent 3D porous rGO film. c,d) Partially enlarged views of (a) under higher magnification. Reproduced with permission.^[75] Copyright 2016, Wiley.

electrospinning the polymer blends followed by 1) selective removal of the phases and 2) phase separation based on the solvent evaporation in the presence of vapor.^[77] With these methods, nano and micrometric porous fibers with unusual surface structures and unique ribbon-like morphologies using a highly volatile solvent have been fabricated. McCann et al.^[78] developed porous polymer fibers through a combination of electrospinning and freeze-casting techniques through an immersion of a collector in a cryogenic liquid (**Figure 9**). Generally, during electrospinning, the liquid jet is basically drawn into the collector, and then rapid solvent evaporation could solidify the fiber and prevent a varicose breakup. However, when freeze-casting was added to the electrospinning process, the fibers were collected in a liquid nitrogen bath prior to reaching the collector. In this case, the remaining solvent was frozen throughout the electrospun polymer. In the freezing process, phase separation into solvent-rich and solvent-poor regions was occurred.^[78] The electrospun and frozen fibers were kept under liquid nitrogen until they were dried in a vacuum. By controlling solvent evaporation, a porous morphology was easily induced in a single step. The extent of porosity but also fiber diameter could be large tuned with controlling the amount of residual solvent which can, in turn, be controlled by changing the collection distance. With this technique, a variety of porous fibers out of different polymers, such as poly(acrylonitrile) (PAN), polystyrene, poly(vinylidene fluoride), poly(ϵ -caprolactone), and so on could be formed.^[78] These porous fibers can potentially be used for various applications such as, encapsulation of active substances, catalyst supports, lightweight reinforcement agents, tissue engineering scaffold, and controlled release of drug molecules.^[79]

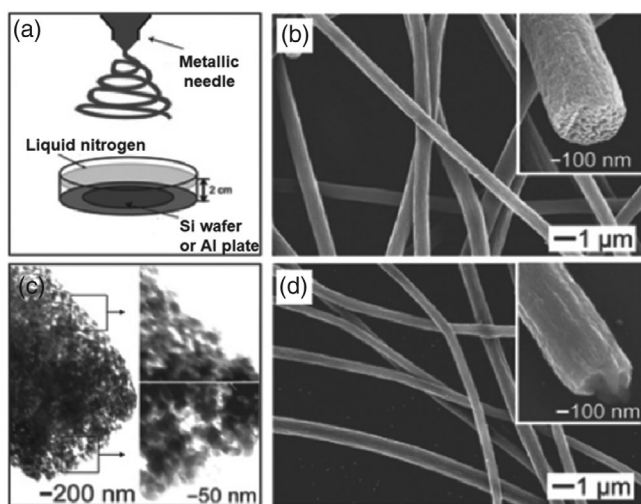


Figure 9. a) The electrospinning setup with the modified collector containing liquid nitrogen. b) SEM images of poly(styrene) porous fibers prepared by electrospinning into liquid nitrogen, followed by drying in a vacuum. c) TEM of the porous poly(styrene) fibers shown in (a) with insets at higher magnification. d) Poly(styrene) fibers electrospun from the same solution into liquid nitrogen but then reheated rapidly to room temperature in the air. Reproduced with permission.^[78] Copyright 2006, American Chemical Society.

3.4. Beads/Microspheres

In addition to bulk monoliths, (e.g., cylinders) of GO, micrometer- to millimeter-sized spherical-shaped 3D aerogel microsphere have also been produced for some particular applications, such as superabsorbent, drug/catalyst carriers, and filter membrane to name only a few.^[72,80] Most of the reported works in this context are based on the composite of GO with a secondary phase, usually a polymer or biopolymer. In this regard, carbon aerogel microspheres formed using sol-gel polycondensation of a resorcinol-formaldehyde solution has indicated an excellent adsorption capacity toward phenol.^[81] Cai et al.^[82] proposed a straight forward spray-freeze drying method to fabricate aerogel microspheres out of cellulose nanofibrils as a novel cell-based scaffold with low bulk density, high moisture, and water absorption capacity. Recently, the novel GO microsphere with center-diverging microchannel has been developed through a combination of electro spray processing and freeze-casting.^[80c] The size of the GO microsphere was adjusted with adjusting the electro spray parameters, mainly flow rate, and liquid properties. The average diameter of the GO microsphere increased from 183 to 413 μm , with increasing the flow rate from 3.75 to 11.25 mLh^{-1} . Yu et al.^[80a] have developed hierarchical honeycomb-cobweb-structured GO/chitosan (CS) aerogel microspheres (average diameter $\approx 200 \mu\text{m}$) with radially oriented microchannel porous structures for water purification by combining electro spraying with freeze-casting techniques (**Figure 10i**). CS has been assembled with GO to form composite blocks by electrostatic interaction and chemical functionalization through controlling the pH. The stable GO/CS suspension loaded into the electro spraying syringe, and with applying a high voltage, the GO/CS microdroplets collected inside the *n*-hexane coagulation bath, where the temperature is maintained at -84°C by liquid nitrogen. The final spherical microdroplets have been prepared after the removal of *n*-hexane by vacuum filtration and lyophilization. Due to the radially oriented pore microchannel inside the microsphere (**Figure 10ii**), rapid diffusion of pollutants, namely organic dyes and heavy metal ions with satisfactory recyclability for GO/CS aerogel microspheres, have been observed.

4. Application of Directional Freeze-Cast Materials

The porous networks with an ordered cellular morphology obtained through directional freeze-casting techniques have been applied to several high-performance/advanced applications, such as materials for thermal energy management,^[22b,26b] piezoresistive-based pressure sensor,^[27b] sorption media for capturing air (e.g., particulate matter 2.5 [$\text{PM}_{2.5}$])^[83] and water pollutants (e.g., oils and organics),^[17,51b] 3D biomimetic scaffold for regenerative medicine,^[29a,82] and porous electrodes for energy conversion and storage.^[58b,84] For most of the aforementioned applications, maintaining mechanical resilience with reversible or cyclic compressibility, while still being highly porous, is very important and at the same time, very challenging. Nevertheless, considering the versatility of the directional freeze-casting technique for cryoassembly of porous materials originating from various building blocks with a possibility of tuning

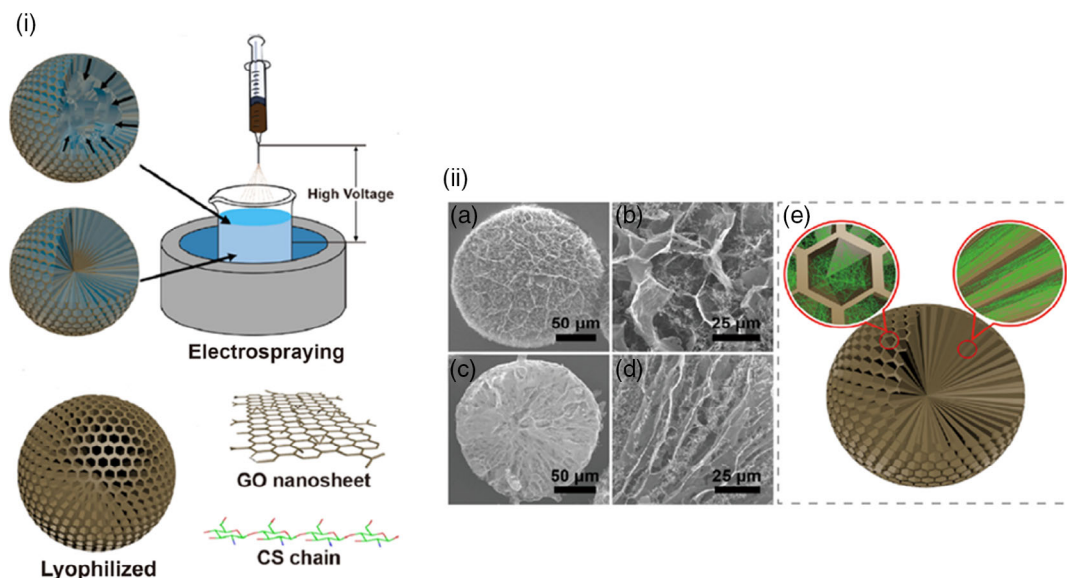


Figure 10. *i)* Preparation scheme of GO/CS aerogel microspheres. *ii)* SEM images of the microspheres and their cross-section (a–d), as well as schematic of GO/CS microsphere with honeycomb–cobweb and radially oriented microchannel structures (e). Reprinted with permission.^[80a] Copyright 2017, American Chemical Society.

micromorphology and mechanical strength, all the proposed applications are feasible.

4.1. Thermal Insulating/Management

With the increasing demands on energy efficiency, a great deal of effort has been dedicated to designing high performance thermally insulating materials in the field of aerospace, building, and construction and wearable devices.^[22a,85] In this regard, lightweight, mechanically, and thermally stable superinsulation materials have granted the urgent requirement of the aforementioned applications.^[26a]

In addition to the traditional insulation materials, such as polyurethane (thermal conductivity $[\lambda] = 20 - 30 \text{ mW m}^{-1} \text{ K}^{-1}$), porous aramids ($\lambda = 28 \text{ mW m}^{-1} \text{ K}^{-1}$), expanded polystyrene (EPS, $\lambda = 30 - 40 \text{ mW m}^{-1} \text{ K}^{-1}$), and polymer/clay aerogel ($\lambda = 45 \text{ mW m}^{-1} \text{ K}^{-1}$) with high thermal conductivities,^[22a,26a,86] emergence of nanomaterials have opened up new opportunities to fabricate more efficient insulating materials.^[87] The 1D and 2D nanomaterials like nanotubes, nanowires, nanorods, and nanosheets can significantly reduce solid heat conduction based on phonon scattering effects.^[88] The nanoporous materials like silica aerogel ($\lambda = 17 - 21 \text{ mW m}^{-1} \text{ K}^{-1}$) have also indicated super-insulating properties, but their fragility made them prone to thermal insulation failure. To solve this drawback, aerogel-based thermal insulators out of various biopolymers, such as polysaccharides (cellulose: $0.015 \text{ mW m}^{-1} \text{ K}^{-1}$, pectin: $0.016 \text{ mW m}^{-1} \text{ K}^{-1}$, chitosan: $0.022 \text{ mW m}^{-1} \text{ K}^{-1}$, etc.),^[89] and protein (silk fibroin: $0.22 \text{ mW m}^{-1} \text{ K}^{-1}$)^[90] have been proposed as better alternatives to the traditional silica aerogels because of their high mechanical flexibility.

Strategies based on the hierarchical assembly have also been proposed to develop porous foams or aerogels with a promising

set of mechanical and thermal insulation properties for a perspective of thermal energy management. In this context, Peng et al.^[26b] developed lightweight, super-insulating, and antifrosting GO/polyimide (GO/PI) foam through UFC of the GO, water-soluble polyimide (PI), and modified polystyrene sphere (PS). PS spheres were incorporated to rGO/PI composite as sacrificial templates and were removed upon thermal annealing to form hollow spherical structures on the cell walls of the nanocomposite. As it is evident from microstructural analysis by SEM analysis of rGO/PI/PS nanocomposite foam (Figure 11), UFC rendered the composite with hierarchical honeycomb-like structure in the perpendicular (*P*) direction to the ice growth and aligned tubular structure along the direction of ice front/axial (*A*). While GO nanosheets contributed to the low density of insulating monolith, PI was incorporated as a reinforcement agent for improving the low mechanical strength of GO foams and enhanced thermal stability. The hollow spherical structures of PS templates on the honeycomb walls of rGO/PI nanocomposite could strongly hamper thermal transport and thus led to ultralow thermal conductivity. In addition, composite showed an interesting surface hydrophobicity with a high contact angle of 138° . As shown in Figure 11iii,iv, the strong microstructural orientation in the resulting composite offered exceptional anisotropic thermally insulating properties so that sample shows two different heat transfer behaviors in *A* and *P* directions. In *P* direction, the GO-modified hollow spherical configurations attached to the pore walls of the sample play a role of air pockets and therefore prevent the thermal transport between the layered structure of composite. Thus, thermal conductivity decreased from $19 \text{ mW m}^{-1} \text{ K}^{-1}$ in *A* direction, to as low as $9 \text{ mW m}^{-1} \text{ K}^{-1}$ in the *P* direction. In addition, compressive mechanical strength has also indicated an anisotropic behavior for both *P* and *A* directions (Figure 11v),^[26b] so that composite showed a wood-like compressive behavior in the *A* direction due the alignment of microstructures upon UFC.

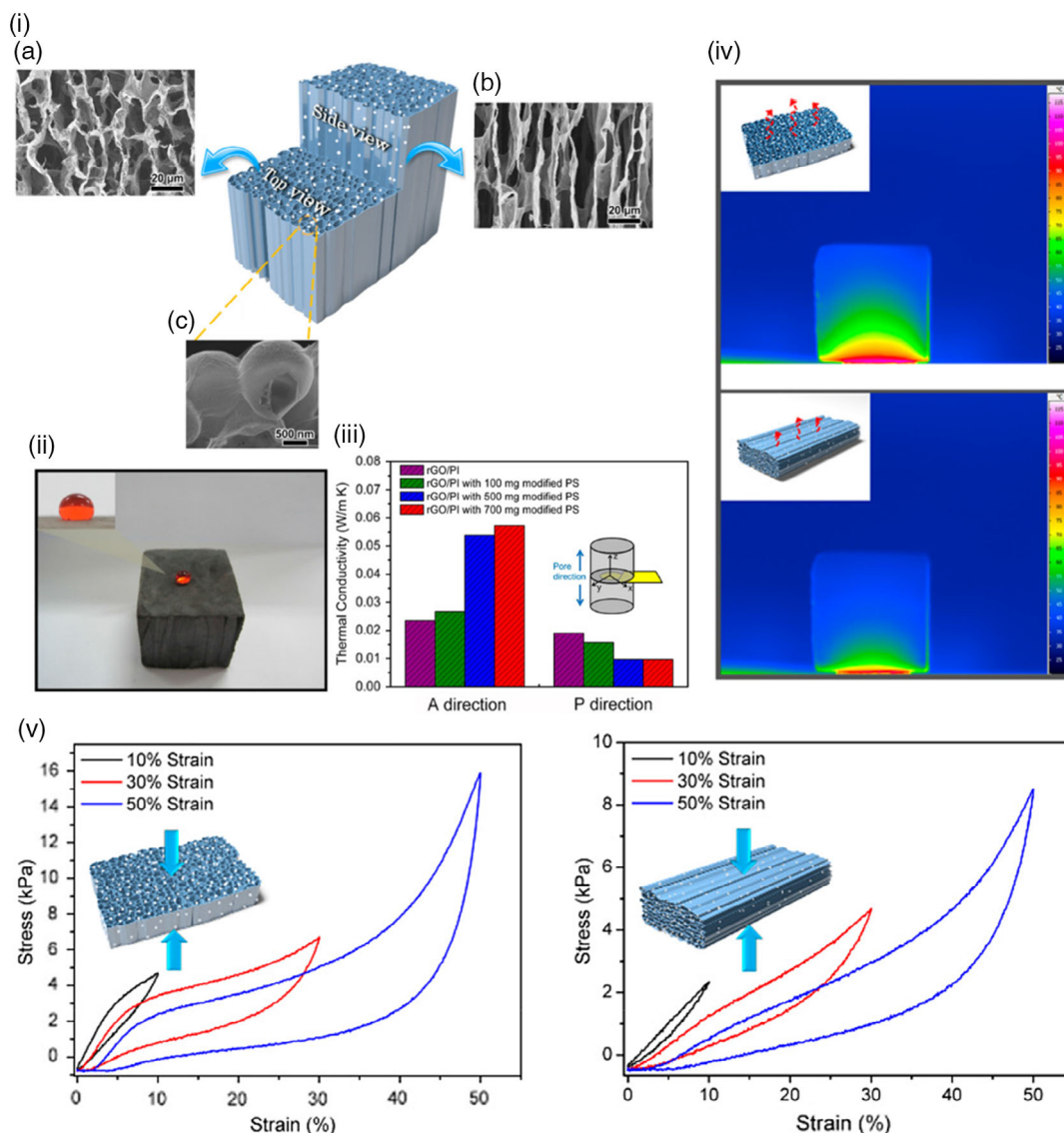


Figure 11. i) High-magnification SEM images of nanocomposite foams in different directions. a,b) SEM images of nanocomposite foams from top and side views, and c) SEM images of secondary hollow spherical structures. ii) Photograph of a water droplet (labeled by red ink) on the surface of nanocomposite foam with a water contact angle of 138° . iii) Thermal insulation properties of anisotropic nanocomposite foam with a comparison of thermal conductivities of rGO/PI nanocomposite with different contents of modified sacrificial PS spheres in directions along (A direction) and perpendicular to (P direction) the growth direction of ice. iv) Thermographic images of the foam in A and P orientations. v) Stress–strain curves for nanocomposite foam with different set strains in A and P directions. Reprinted with permission.^[26b] Copyright 2017, American Chemical Society.

The anisotropic freeze-casting method has also been used to create unidirectional channels in porous ceramics and carbonaceous structures with the purpose of increasing the thermal conduction for some application purposes, namely advanced electronic packaging with efficient thermal dissipation.^[18b,26c] For instance, vertically aligned and interconnected graphene networks (VAIGNs)–epoxy composites have been developed through freeze-casting of aqueous solution and annealing reduction under Ar.^[18b] VAIGNs–epoxy composites with honeycomb-like pores on the wall exhibited better thermal transport in the direction of ice growth compared with the randomly oriented graphene–epoxy composites. However, the freezing method,

concentration of GO solution, and the reduction method all played a role in determining the formation of the final VAIGNs structure.^[18b]

Wicklein et al.^[22b] have also shown that freeze-casting of the suspension of cellulose nanofiber, GO and sepiolite nanorods (SEPs) can form an anisotropic, nanoporous composite foams with combination of very low radial thermal conductivity ($15 \text{ mW m}^{-1} \text{ K}^{-1}$), high axial specific Young's modulus (77 kNm kg^{-1}), and good fire retardancy (Figure 12i,a,b). The addition of SEP to the nanocellulose provided the nanocomposite with higher specific mechanical strength in the axial direction with good moisture resistance. By adjusting the freezing

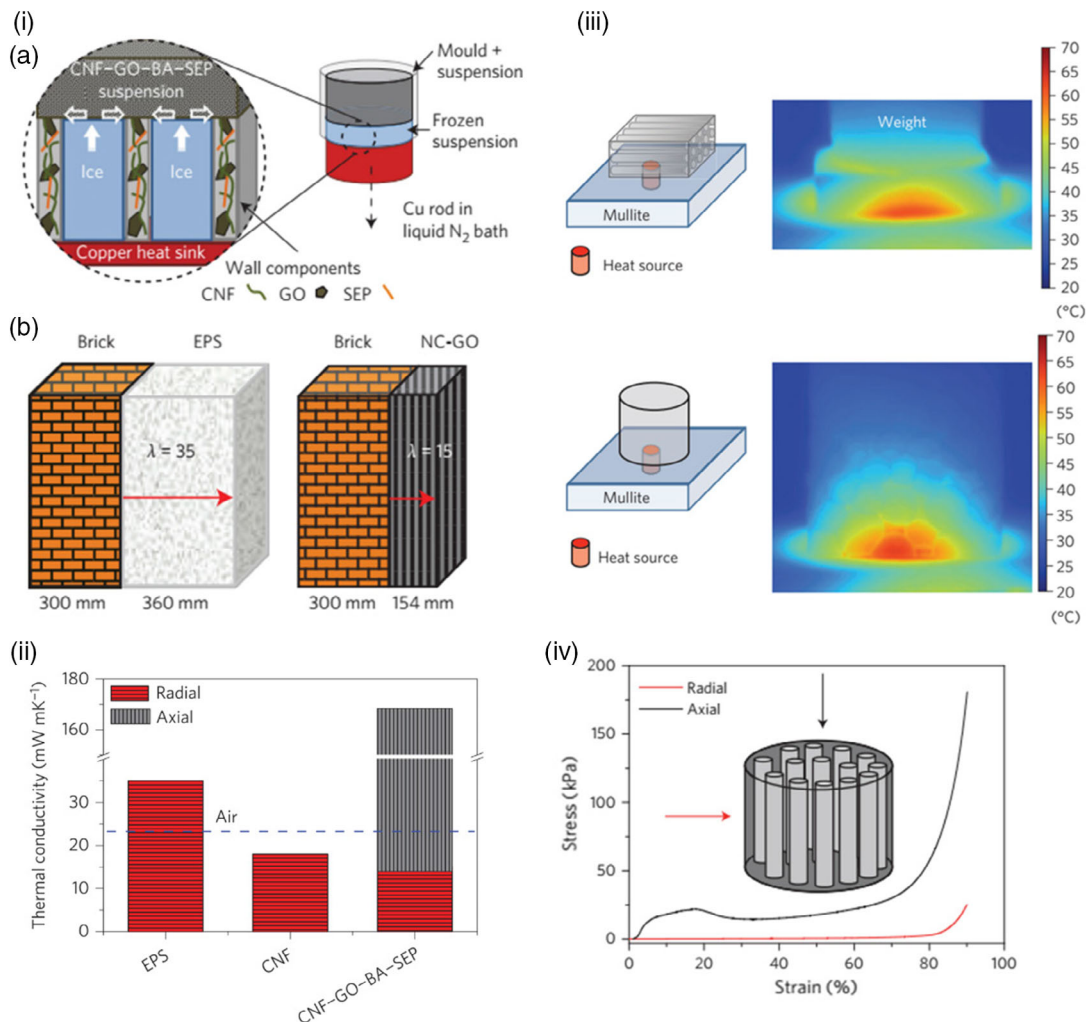


Figure 12. *i*,a) Fabrication of CNF-GO-BA-SEP-based nanocomposite foam through the freeze-casting process, highlighting the growth of anisotropic ice crystals surrounded by walls of the dispersed nanoparticles (not drawn to scale). *i*,b) Schematic illustration of the thickness of EPS and an optimized nanocomposite foam needed for passive house insulation (energy loss ≤ 100 mW m⁻¹ K⁻¹). The thicknesses of the brick and insulating layers are given in millimeter and calculated using λ values of 35 and 15 mW m⁻¹ K⁻¹ for EPS and the nanocellulose-graphene oxide (NC-GO)-based composite foam, respectively. *ii*) Thermal conductivity values in the axial and radial directions of CNF and CNF-GO-BA-SEP foams, compared with EPS. *iii*) Thermographic images of CNF-GO-BA-SEP nanocomposite foam with the tubular pores oriented normal to the heat source and a closed-cell EPS foam. The heated volume of the CNF-GO-BA-SEP nanocomposite foam is smaller and more homogeneous than that of the EPS foam. The colors in the thermographic images show the temperature distribution on the surface of the foams. *iv*) Stress-strain measurements of a nanocomposite foam containing 77% CNF, 10% GO, 10% SEP, and 3% BA (in wt%), determined in both the strong and stiff axial orientation and the much weaker radial orientation with respect to the tubular pores. Reprinted with permission.^[22b] Copyright 2014, Nature Publishing Group.

conditions, high control over pore orientation, size, and density were obtained. Authors of this work found that in the higher cooling rates, the smaller pore diameters were created. The thermal conductivity of the freeze-cast nanocomposite foam was significantly lower than those of traditional insulation materials, such as EPS and polyurethane with exhibiting substantial anisotropy toward the direction of ice growth (Figure 12*ii,iii*). The stress-strain curves from compression studies at different axial and radial directions in Figure 12*iv* show the typical deformation behavior of an open honeycomb-like foam. The foam showed a linear elastic behavior at low strain, a cell-collapse stress reduction at moderate strain

and a plastic yielding plateau with subsequent stiffening at high strain.

4.2. 3D Biomimetic Scaffold for Tissue Regeneration

The synthesis of 3D networks to mimic the porous matrix of tissues for cell attachment and growth is a big challenge in the field of tissue engineering. Scaffolds with interconnected pores and sufficient strength to prevent crushing under physiological loads during the integration and healing process have intensively been investigated over the past decade.^[91] An ideal 3D substitute should be capable of forming secure bonds with

surrounding tissues while allowing new cells to penetrate and grow along with the exchange of nutrients and oxygen.^[92] Porous scaffolds are highly recommended for this goal as cells can desirably grow within the pores to prevent the movement of the implant. In addition to the pore size and surface chemistry of the scaffolds, considerable attention has recently been given to the morphology of the porous structure as a determining factor in successful tissue regeneration.^[93] Investigations have recently been shifted toward the development of favorable techniques that can produce highly porous morphologies with controlled size and orientation in a repeatable, reliable, and economical way. Nevertheless, many of these techniques are still suffering from the inherent lack of scaffold strength due to the high porosity, limiting their application to low-stress locations, such as fractured skulls and broken jaws.^[94] Therefore, the design of highly porous scaffolds with high resistance to mechanical pressure has remained still an unresolved dilemma despite a plethora of investigations on the creation of 3D scaffolds with regular or irregular pore orientation.

Different polymers, such as collagen, chitin, gelatin, polylactic acid (PLA), poly(lactide-co-glycolide) (PLGA), poly(2-hydroxyethyl methacrylate) (poly(HEMA)), agarose, sericin, and alginate have been studied for the synthesis of scaffolds by UFC.^[79,95] Although not strong enough for tissue regeneration in load-bearing locations of the human body, all these structures had homogeneous open pores for rapid cell attachment and proliferation. In the field of tissue engineering, the scaffolds developed by UFC have mainly attracted the attention of scientists for bone regeneration.^[96] For example, Maleki et al.^[29a] enhanced the mechanical strength of aerogels through freeze-casting and successfully achieved the efficient formation of bone in an animal model. They prepared a 3D scaffold through a one-pot aqueous-based sol-gel assembly of organosilane (tetraethyl orthosilicate) and silk fibroin (SF) biopolymer, followed by UFC of the gel and supercritical drying to construct ultralight silica-SF aerogels with hierarchical porous structure. Honeycomb-shaped anisotropic pores (Figure 13i,a) were a desirable place for the attachment, growth, and differentiation of osteoblast cells, acting as a very competent matrix for bone tissue formation. As shown in Figure 13i,b, ALP activity (the early marker of bone cell differentiation to osteoblast phenotype) of MG-63 cells cultured on the scaffold and β -tricalcium phosphate (TCP) showed meaningfully higher alkaline phosphatase (ALP) activity for the cells seeded on the scaffolds than the blank TCP at each time point. In addition, induced bone formation was observed in vivo in the bone defect site of an animal model in 25 days postimplantation. Figure 13i,c shows the macroscopic images of the new bone formation around and inside the implants. The integration of the scaffold into bone microstructure was observed in the scaffold-receiving group without any harmful effect on the surrounding tissues. In fact, high safety and osteoconductive nature of the silica-SF scaffold hindered degenerative reactions and necrosis in the defect site and boundaries of the implanted scaffold. The scaffold was desirably accepted by the local bone tissue without complications, such as inflammation, bleeding, or infection. In contrast, necrosis and cellular degeneration were observed in the bone defect site of the femur of animals that did not receive scaffold implantation. This study can be considered as an inspiring work for the future development of biocompatible scaffolds using a variety of

materials, such as ceramics, synthetic and natural polymers, and proteins, as well as various manufacturing technologies to develop scaffolds with aligned porosity to resemble biological and physicochemical properties of the bone tissue. In fact, unidirectional micrometer-sized pores obtained by freeze-casting would render cell ingrowth and spreading on the scaffold, whereas nanopores inside the polymeric wall of the scaffold would allow signaling communication of cells, nutrition delivery, excrements' removal potential, mechanical stability, and flexibility. Moreover, hierarchically organized porosity obtained by freeze-cast scaffold is beneficial for in vivo neovascularization and formation of the hydroxyapatite-rich cement line in the early stage of osteoconduction, especially when bioactive agents, such as silica is incorporated within the matrix of the scaffold. For example, silica/chitosan scaffold with oriented pores has been fabricated through the sol-gel method through the UFC process.^[98] In this study, the cooling rate during the freezing process was recognized as an effective factor in tailoring the mechanical properties of the scaffolds. While being bioactive due to the presence of silica within its structure, this scaffold was elastomeric and flexible perpendicular to the freezing direction and behaved in an elastic-brittle fashion parallel to the freezing direction. This is a unique criterion that would allow clinicians to squeeze the scaffold to fit tissue defect sites, while providing some mechanical support from the other direction. This scaffold was suggested as a good candidate for bone tissue regeneration as it could bond to bone, stimulate bone growth, and degrade in the body in a tailored manner; however, its brittle nature would not allow its usage for bone defect sites that are under cyclic or multidirectional loading. In contrast, it was suggested as a promising biocompatible 3D structure for bone defects that strong mechanical properties dominant in one direction are needed. However, in addition to biocompatibility, suitable biodegradability within the body is another necessary criterion of freeze-cast scaffold for in vivo applications. Therefore, scientists have recently started to develop biodegradable scaffolds by freeze-casting method not only for bone tissue engineering, but also the regeneration of damaged soft tissues by the design of elastomeric porous scaffolds with adjustable mechanical properties. For example, chitin nanocrystal (ChiNC) and poly(1,8-octanediol-co-pluronic F127 citrate) (POFC) prepolymer have been used to construct a pickering-like emulsion, which could create a nanoreinforced porous elastomeric scaffold after undergoing freeze-casting process (Figure 13ii,a).^[97] The presence of citrate was assumed to endow the scaffold with suitable surface affinity toward cells for tissue engineering applications.^[99] In addition to its emulsifying role to stabilize POFC latex spheres, ChiNC also played a key role in preventing the collapse of ice-templated pores during thermocross-linking and also reinforced the mechanical properties of the elastomer porous scaffold. As shown in Figure 13ii,b, while the pure POFC elastomer film showed a rapid degradation, ChiNC containing elastomers delayed the rate of degradation as a result of additional cross-links and chemical bonding between POFC and ChiNC. However, the ChiNC ratio did not have significant effects on the degradation rate of porous scaffolds and nonporous film. Enhanced mechanical property has been also obtained using chemical cross-linkers instead of nano reinforcement approaches. For example, 3D foam scaffolds of cationic

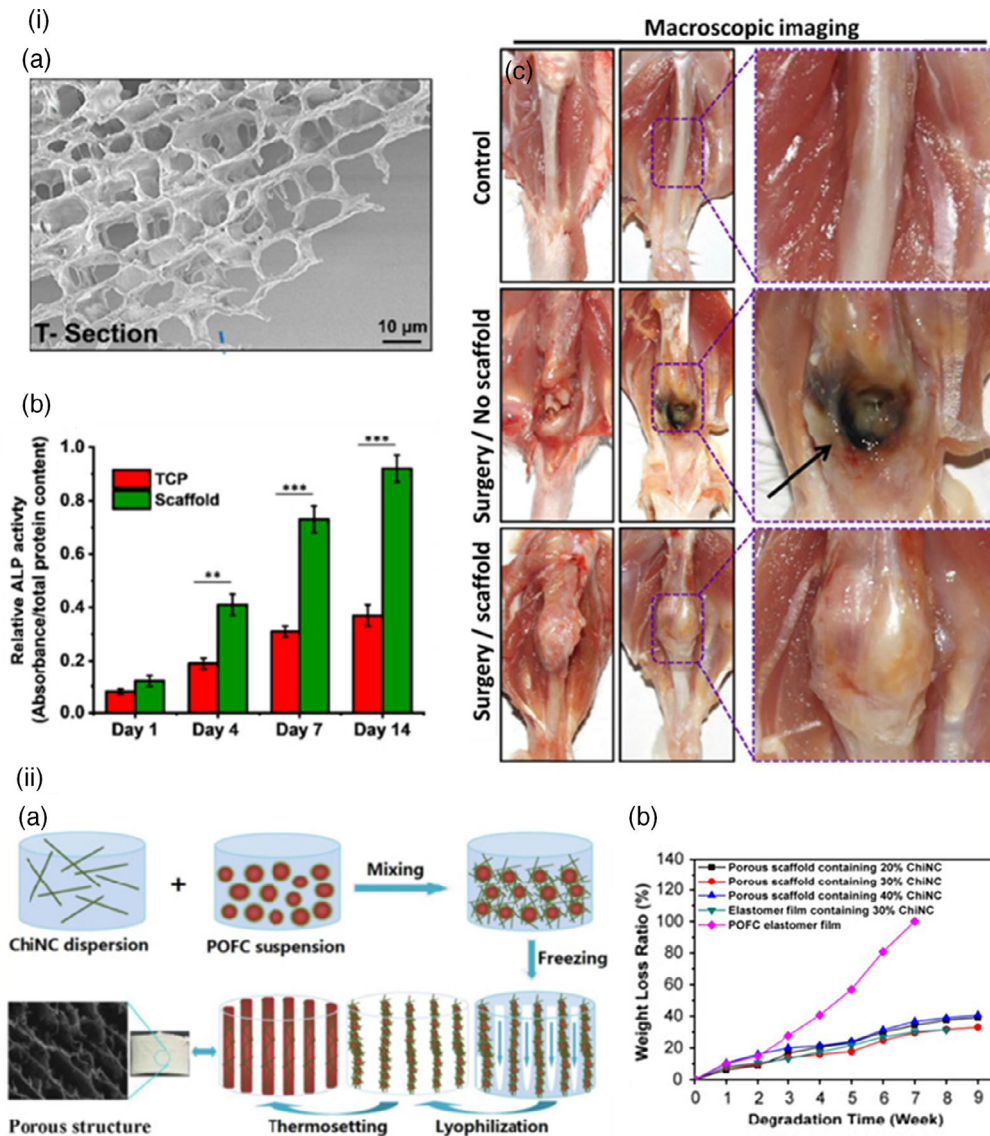


Figure 13. *i,a)* SEM of the microstructural structure of the silica-SF scaffold. *i,b)* ALP activity of MG-63 cells cultured on the scaffold for 14 days. *i,c)* Macroscopic images of the defect region of the rat femur 25 days after implantation of the silica-SF scaffold. Reprinted with permission.^[29a] Copyright 2019, American Chemical Society. *ii,a)* Schematic illustration of fabricating ChiNC supported the POFC scaffold through the emulsion-freeze-casting process. *ii,b)* In vitro degradation of ChiNC-POFC porous scaffolds and elastomer films in PBS medium. Reprinted with permission.^[97] Copyright 2017, American Chemical Society.

cellulose nanofibril (CCNF) with unidirectional channels were obtained by freeze-casting for the mimicking of vascularized tissue^[100] when glyoxal was used to promote mechanical property of the CCNF by making strong cross-linked bridges among the cellulose backbone. The viability of MG-63 cells was increased in the glyoxal cross-linked CCNF scaffolds and could provide robust foams for 3D cell culturing through the mimicking of ECM.

In general, preparation of hierarchical scaffolds by freeze-casting for tissue regeneration is in its infancy and we believe this field will grow up rapidly in the coming years as there are plenty of natural and synthetic polymers, which can be used to form novel hybrid scaffolds by this technique to achieve high porosity, high surface area, and improved anisotropic

mechanical behavior. At the moment, there is no investigation on how the surface modification of freeze-cast scaffolds by peptides and proteins can change its behavior and effect on cells. Therefore, comprehensive works are needed to understand the combined effect of surface modification and aligned porosity of such scaffolds on tissue regeneration.

4.3. Pressure (Piezoresistive) Sensors

The piezoresistive-based pressure sensors work with converting mechanical forces to the electrical signals (e.g., changes in electrical resistance).^[27b] In the field of the piezoresistive-based pressure sensors, as creating an electrical conduction path is highly

required for the functioning of the developed sensors, most of the devices proposed so far have relied on using electrically conductive starting precursors, usually 1D and 2D carbon allotropes^[54,57] and ceramics.^[101] In these sensors, the resistance changes in a porous matrix upon the compression process due to the variation in the conducting paths and contact resistance between the closely located cells or pore walls. Several piezoresistive sensors based on, MXene/reduced GO hybrid 3D foam,^[101] super flexible polyimide/rGO aerogel,^[27b] and nacre-mimetic rGO/PVA porous film^[102] have been proposed, which all have shown great promises in the transduction of cyclic compression to resistance changes even at ultralow (<1 Pa), subtle (1 Pa–1 kPa), and low pressure (1–10 kPa) ranges.^[103] Zang et al.^[103] have well-reviewed all the flexible pressure sensor devices fabricated by various functional materials and their sensing performance optimization. It has been shown that unlike the pristine isotropic graphene or CNT aerogels prepared by random stacking, which are easily collapsed when subjected to compressive stress,^[104] the free-standing ultralight multiwall carbon nanotube (MWCNT) aerogels that were fabricated by a UFC approach, with an ordered honeycomb-like structure, possessed excellent compression recoverability.^[105]

As the ultimate properties of porous materials are determined by the intrinsic properties of their constituents and final structural geometry, the same mechanical resilience as MWCNT aerogel was also observed for cellular macrostructures developed by the hybridization of MWCNT and graphene upon directional freeze-casting.^[106] The MWCNT/GO structures have been formed using a UFC approach to assemble network constituents in an ordered and hierarchical manner. As shown in **Figure 14i–iv**, by mixing these two types of building blocks, ordered honeycomb-like microstructures with joint walls in the growth direction have been obtained in the final hybrid foams. The remarkable mechanical performance (>2000 loading-unloading cycles) in the ultimate MWCNTs/GO hybrid foam (**Figure 14ii**), has been attributed to the highly organized, multiscaled hierarchical architectures at different levels, which caused a dynamic cell wall strength and stability. In addition to honeycomb-like morphology in the transverse direction, the obtained foams exhibited an anisotropic channel-like morphology in the longitudinal direction, with the pore size in the order of tens of micrometers. By increasing the pressure up to 2.5 kPa, the resistance variation ($\Delta R/R_0 = (R_p - R_0)/R_0$, where R_0 and R_p are the electrical resistances without and with applied pressure, respectively) was increased until the increasing trend of $\Delta R/R_0$ became trivial with applied pressure (**Figure 14iii,a**). Here, the decrease in the resistance upon foam compression is due to the reduction of the conducting paths and contact resistance upon compression of the pores or cells in foam.^[106] Due to the unique resilience performance combined with electrical conductivity, the sensor could sense and detect the pressures as low as 36 Pa (subtle pressure) (**Figure 14iii,b**), and therefore has been integrated into pixel arrays for building an ultrasensitive artificial electronic (e)-skin (**Figure 14iv**).

Generally speaking, the ordered organization of microstructure and/or generation of honeycomb micromorphology in the hybrid foams could lead to uniform deformation upon compression, and therefore elasticity upon compression can be increased. Whereas in the randomly structured foam, due to the

nonuniform distribution of the pore size, inhomogeneous strain, and remarkable local deformation could be observed.^[106]

4.4. Pollutants' Sorption by Unidirectionally Freeze-Cast Materials

The aligned channels/pores obtained by directional freezing render the structure of the material with a potentially superior configuration for performing as an absorbent for treating the contaminated water with oils and organic solvents.^[107] The absorption capacity obtained for aerogels' configuration through directional freeze-casting has been reported superior to the "traditional" aerogels made by conventional templating techniques with an inhomogeneous porous structure.^[17] In this regard, anisotropic aerogels in various morphologies, namely in microparticles/beads and monolith forms obtained with directional freeze-casting, have been investigated for selective absorption of oils, metal ions, and dyes from water.^[23,51b,52a,53a,80,95h] Recently, we have comprehensively reviewed the sorption performance of various aerogels for different water and air pollutants via absorption and (photo) catalytic abatement mechanisms.^[108] For example, as already mentioned in Section 2, the centrosymmetric/radially assembling of the GO sheets into the aligned structure through bidirectional freeze-casting has resulted in a mechanically robust and elastic aerogel for the absorption of different organic pollutants from water.^[17] The recyclability toward repeated absorption of organic moieties has also been studied through the absorption–combustion rout. The bidirectional freeze-cast rGO aerogels exhibited the largest absorption capacity of 374.7 g g⁻¹ for carbon tetrachloride. As the author claimed, the driving force for the absorption and transmission of organic solvents into the aerogel body was the capillary effect.^[90b] The capillary effect was even more dominant when the capillary channels became narrower. In addition, compared with conventional rGO aerogels with inhomogeneous porosity, the organic solvents could be more readily uptaken by the pores of the anisotropic rGO aerogel by capillary tension forces (**Figure 15i**).

Microparticles or spheres or beads,^[80,81] developed by electrospraying as well as conventional dripping associated with freeze-casting techniques, have also been used for water treatment purposes. In this regard, Yu et al.^[80a] developed GO/CS composite aerogel microspheres (GCAMs) with radially oriented microchannel structures through electrospraying combined with freeze-casting techniques for the adsorption of heavy metal ions and soluble organic pollutants. CS was assembled with GO to create a composite structure by electrostatic interaction as well as covalent bonds, thus enhancing the stability of GO aerogels in aqueous solutions. The hierarchical honeycomb structures in the developed microspheres rendered high adsorption capacities toward heavy metal ions, cationic and anionic dyes, and organic solvents. This high absorption capacity was attributed to the radially oriented microchannels inside the microspheres, which could remarkably shorten the internal diffusion path, thus facilitating rapid diffusion and enhancing the adsorption rate.

In another study by Ouyang et al.,^[80b] GO sheets with CS have been assembled into ≈3 mm diameter core–shell beads with controlled microstructure hybrid spheres. As shown in **Figure 15ii,a**, the spherical core–shell particles were

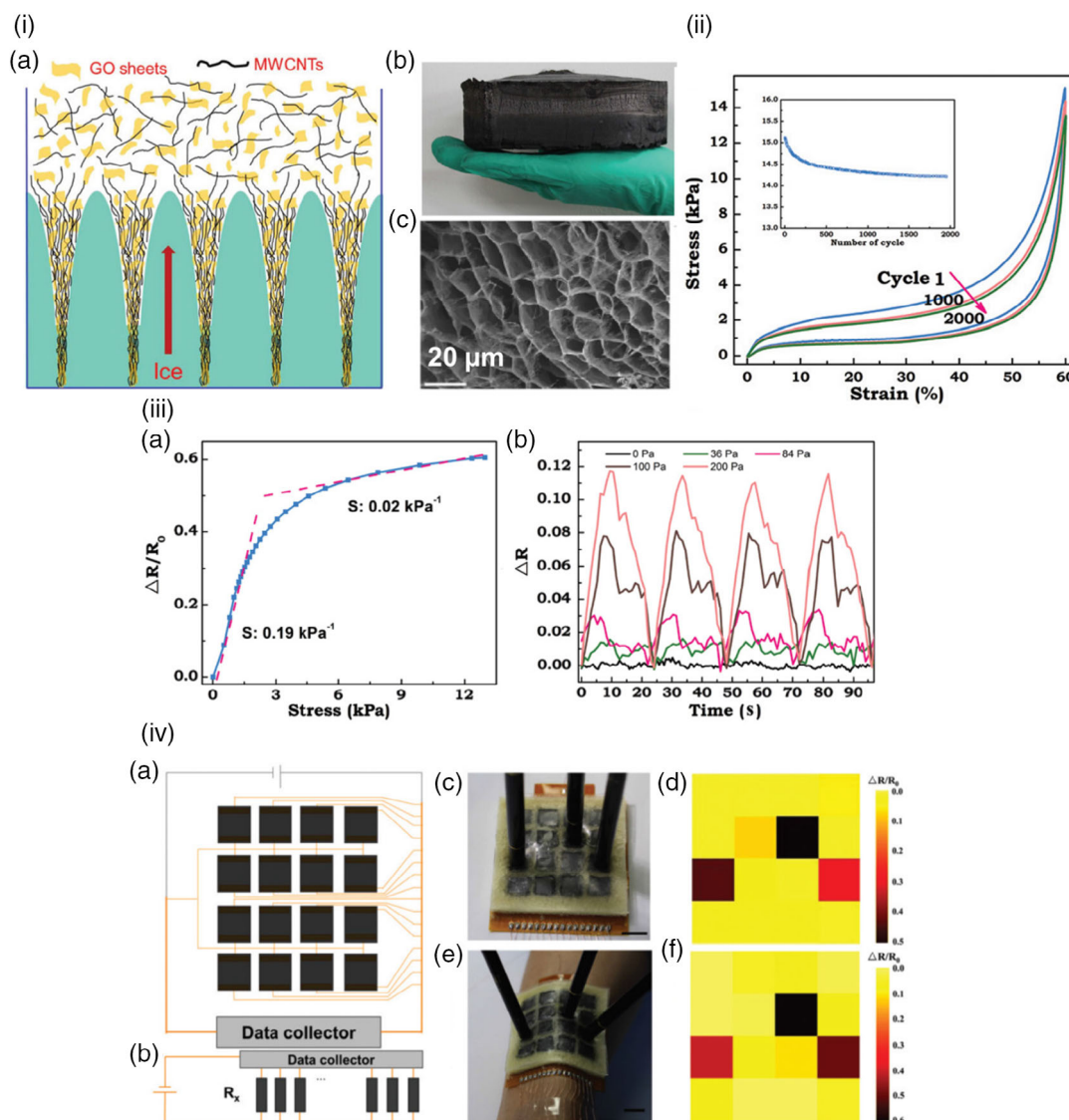


Figure 14. i) Illustration of the fabrication technique of a) MWCNTs/GO hybrid foams b) with digital images of the corresponding sample, and c) with its cross-sectional SEM micrograph. ii) Stress–strain curves of hybrid foam at 1st, 1000th, and 2000th cycles during repeated compression to 60%. iii) Characterization of the resistive pressure response of hybrid foam. a) Electric variation ratio changes with applied pressure and b) detection limit test on the hybrid foam. iv) Schematic model of the artificial skin: the hybrid foams (black squares) were attached to the electrodes (yellow rectangles), and the signals were collected by the data collector. Reprinted with permission.^[106] Copyright 2015, Royal Society of Chemistry.

synthesized through stepwise freeze-casting techniques, in which GO sheets were first assembled into the spheres (core, 1.2 mm) and then underwent to the second freezing step to cover with a layer of CS with a thickness of 0.6–0.8 mm (Figure 15ii,b). The core–shell particles were highly porous (94–96% with a mesoporous volume of $\approx 0.246 \text{ cm}^3 \text{ g}^{-1}$) and have shown a better adsorption capacity (353 mg g^{-1} at 318 K) toward methyl orange (MO) than that of CS particles (Figure 15ii,d). The adsorption of dye molecules into the developed spheres was regulated with pH, temperature, sphere dosage, and concentration of absorbate. As shown in Figure 15ii,d, for both CS and core–shell microparticles, a suitable pH for adsorption was acidic and weak alkaline (with adsorption

capacities of nearly 60 mg g^{-1}), whereas in strong alkaline condition (pH up to 12), a significant reduction on the capacities occurred.

4.5. Electrode for Supercapacitors

The unique properties of porous materials, such as large effective surface area (more than $2500 \text{ m}^2 \text{ g}^{-1}$) and ultralightness (less than 20 kg m^{-3}) with a 3D hierarchical porous structure including interconnected pores render them as effective electrodes for the energy conversion and storage systems.^[109] In this regard, the 3D conductive porous materials having a continuous porous structure with low tortuosity guarantee the fast and appropriate

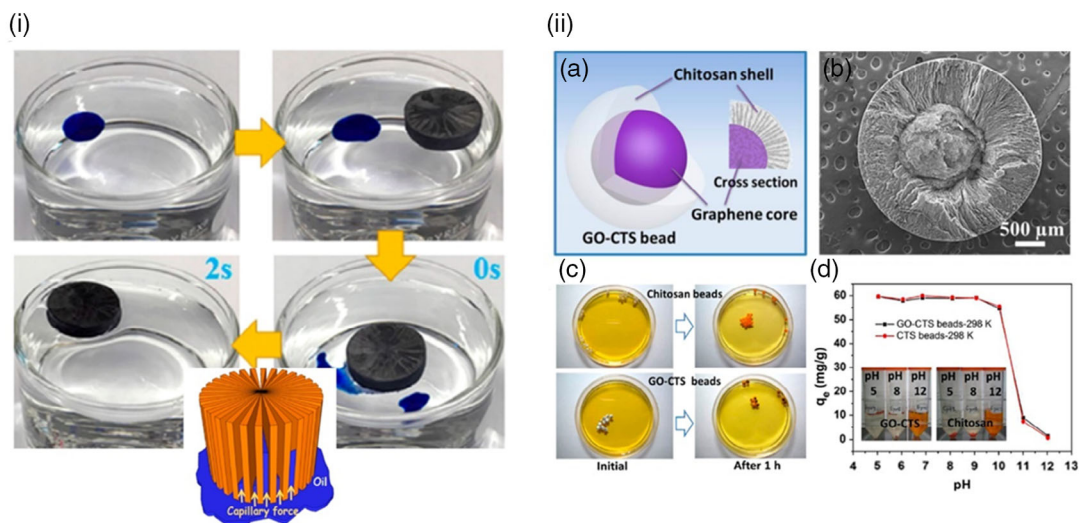


Figure 15. i) Photos show the absorption of an organic solvent (cyclohexane dyed with Unisol blue AS) using as-prepared rGO aerogel obtained with bidirectional freeze-casting with the absorption mechanism model, which shows the directional alignment of capillary flow induced by radially aligned channels. ii, a) Schematic illustration of the 3D core-shell structure of a GO-CTS bead b) together with an SEM image showing a GO core embedded in the CTS shell. c) Adsorption tests for CTS and GO-CTS beads placed in MO solutions at an initial stage and after 1 h of adsorption. The beads have turned to yellow color. d) Adsorption capacity at equilibrium (q_e) versus MO solution pH values for CTS and GO-CTS beads. Reprinted with permission.^[17,80b] Copyright 2018 and 2015, American Chemical Society and Royal Society of Chemistry, respectively.

access of electrolyte and electroactive compounds to reaction sites on the electrode surface, therefore effectively improving the electrochemical performance of the supercapacitors.^[110]

The electrode material plays the main role in supercapacitor's efficiency.^[75] The high electrical conductivity, high temperature, and chemical stability, high effective surface area per unit volume have been identified as essential criteria for the materials used in electrode construction. In this regard, Shu et al.^[84] fabricated a flexible porous graphene (PG) paper that could be directly used for electrode preparation in the absence of any binder or mechanical pressing step. The freeze-dried GO gel was then thermally and chemically reduced. Fabricated PG presented a cross-linked porous structure having a pore size of about several micrometers and a surface area of $148 \text{ m}^2 \text{ g}^{-1}$. It is worthy of mentioning that the morphology of the graphene papers has a significant impact on the desirable properties. When PG was used as electrode material in the lithium-ion battery, it could deliver 1200 mAh g^{-1} discharge capacity and 1056 mAh g^{-1} reversible capacity due to the high number of active sites for lithium-ion insertion in its interconnected 3D porous structure. In addition, the interconnected 3D porous structure of PG, obtained with freeze-casting, facilitated charge transfer and ions, which led to fast rate discharge/charge capability with a capacity of 420 at 2000 mA g^{-1} . PG was also able to maintain 97% of its initial capacity after 100 cycles. Furthermore, PG structure was suggested as a very suitable material for all-solid-state supercapacitor fabrication. The prepared PG paper was proposed as a promising electrode material for the construction of wearable or rolling-up devices regarding its mechanical robustness and flexible structure.

Graphene film having high surface area is a suitable choice for supercapacitor electrode construction if the restack of 2D graphene sheets that led to the formation of dense lamellar material is prevented.^[75] Notably, to achieve rapid kinetics of

electrochemical reactions in a supercapacitor, construction of 3D graphene nanostructure with a high value of open hierarchical pores is demanded to guarantee the presence of ion-buffering repository and dictates rapid-ion diffusion path with fast charging and significant power densities. Shao et al.^[75] developed a procedure for the synthesis of 3D porous rGO film by freeze-casting technique. In their procedure, rGO suspension was partially reduced and converted to a microgel; then vacuum filtration was applied to assemble the as prepared rGO into a film, which further freeze-casting method was used to obtain final 3D porous rGO film (Figure 16). The constructed porous microstructure showed an unlimited linear $I-V$ curve accompanied with high and stable conductivity of 1905 S m^{-1} and the tensile strength of 18.7 MPa , revealing the suitability of its electrical and mechanical properties for supercapacitor construction. Experimental tests revealed an outstanding gravimetric capacitance of 284 F g^{-1} at a current density of 1.0 A g^{-1} , which retained more than 61% of its capacitance at high current density of 500 A g^{-1} , whereas the rGO possessed almost half of the gravimetric capacitance of 3D porous rGO with current density retention of less than 28% at 500 A g^{-1} . 3D porous rGO displayed very large cyclic voltammetry curves area with long discharge time confirming its higher capacitance compared with rGO (Figure 16g).

The ability of long-time cycling performance is an essential parameter for a supercapacitor that 3D porous rGO has this feature very well. The procedure of 3D porous rGO synthesis remains less content of oxygen functional groups such as carboxyl, epoxy, and alkoxy at its carbon structure surface, which is responsible for the appearance of pseudocapacitance properties as a result of Faradaic processes.^[75] The instability of the presence of functional groups and their pseudocapacitance output led to capacitance decreasing during long-term cycling. On the other side, their related Faradaic reactions can restrict the durability

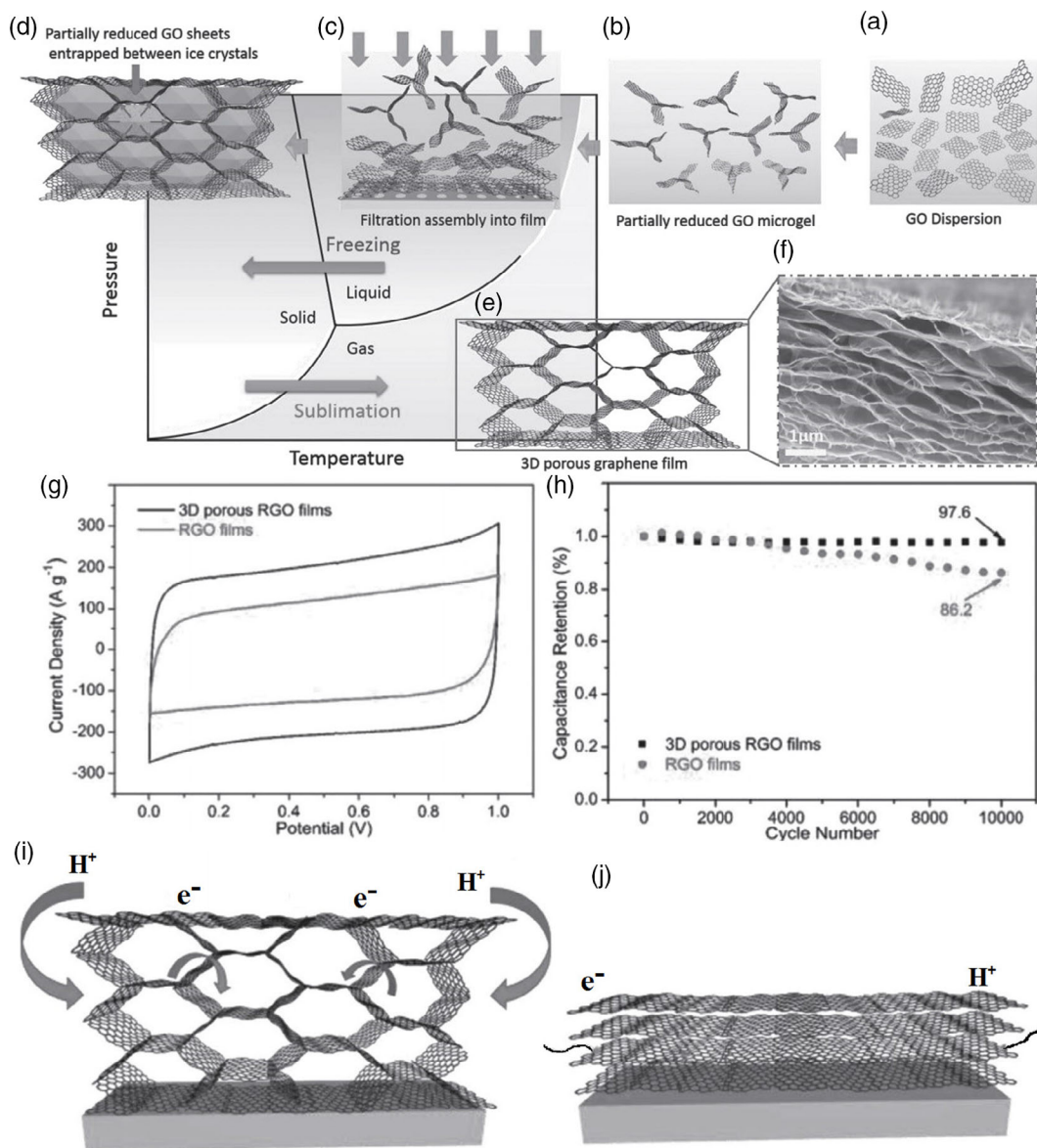


Figure 16. Mechanism of forming a 3D porous microstructure. a–e) Schematic illustration of the formation of a porous graphene film through prereduction, filtration assembly, and freeze-casting. The water phase diagram shows the status of the aqueous solution during different procedures. f) A typical cross-sectional SEM image of a porous graphene film. g) Comparison of cyclic voltammetry profiles for a 3D porous rGO film and rGO films under the same scan rate of 1 V s^{-1} . h) Comparison of cycling stability after 10 000 cycles. i, j) Schematic illustration of ion and electron transport in a 3D porous rGO film and an rGO film. Reprinted with permission.^[75] Copyright 2016, Wiley.

of the aqueous electrolyte. As a result, unlike RGO films, the 3D porous rGO layers possess long-lasting cycling stability without charge loss (Figure 16i,j). The electrochemical impedance spectroscopy (EIS) experiments revealed that the 3D porous rGO film has indicated a low internal resistance and a high charge conductivity which is attributed to its fast electron transfer along the pore walls as well as facile ion migration through the 3D open porous structure. In the absence of any diffusion restriction effect, the ions of the electrolyte can easily migrate to the open porous structure of the 3D rGO network which can then ensure a large capacitance at a high current density/scan rate. Inner resistance to ion

transfers as well as charge transfer resistance have mainly restricted the specific power density of a supercapacitor. Low amount of these two parameters in addition to high capacitance with an ideal electrolyte ion migration could create a very high-power density of 282 kW kg^{-1} and an energy density of 9.9 Wh kg^{-1} for the electrodes constructed of the 3D porous rGO in an aqueous electrolyte. There are several literature reviews which have shown that a combination of metal and metal oxide materials with 3D rGO could produce materials with outstanding properties applicable for the construction of supercapacitors,^[111] high-performance lithium-ion batteries,^[112] and fuel cells.^[25a,113]

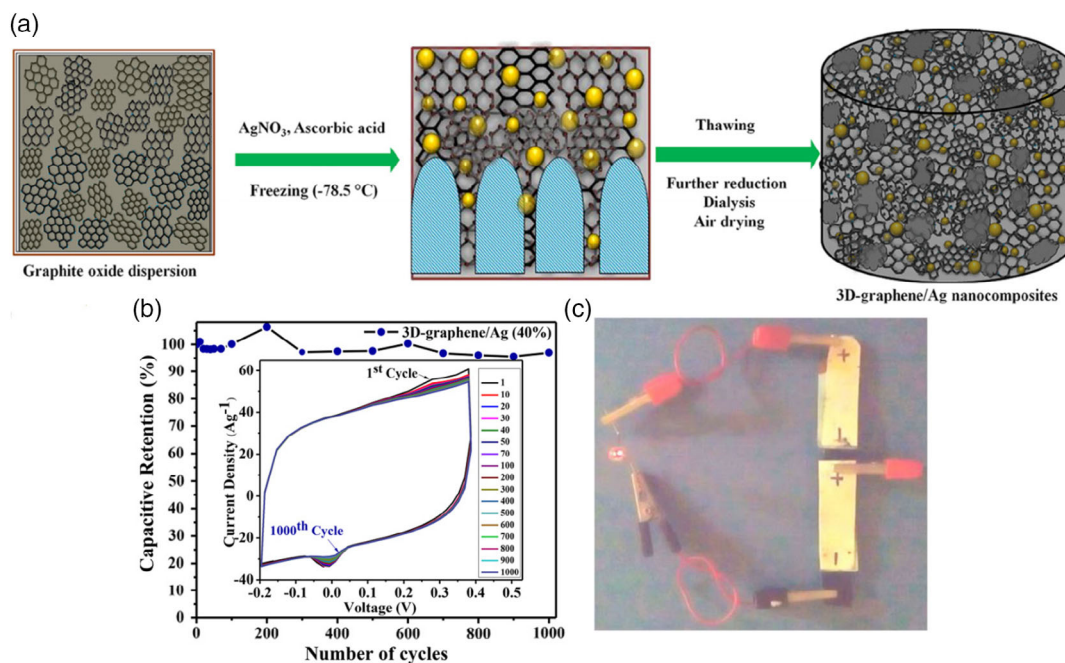


Figure 17. a) Schematic representation for the synthesis and formation mechanism of 3D-graphene/Ag nanocomposites with different loadings of Ag using an air-drying process and their supercapacitor, catalytic, and antibacterial applications. b) Capacitive retention values of 3D-graphene/Ag (40%) at 100 mV s^{-1} scan rate for 1000 cycles (inset shows the corresponding cyclic voltammetry curves) and c) demonstration of two fabricated ASC devices in series that light up the commercial red light-emitting diode (LED). Reprinted with permission.^[114] Copyright 2018, American Chemical Society.

The deposition of noble metal on the 3D rGO prevents the aggregation of nanometals and meanwhile extremes the loading amount that led to nanocomposite with high effective surface area and higher electron conductivity.

Sahoo et al.^[114] has fabricated a 3D open porous carbon-based porous structure as a highly efficient supercapacitor. Considering chemical stability and high electrical conductivity of Ag as a noble metal, they synthesized the Ag nanoparticles decorated 3D rGO via the freeze-casting method (Figure 17). The interconnected porous graphene sheets helped them to synthesize efficient 3D rGO/Ag nanocomposite with about 40% Ag loading via preventing the aggregation of deposited Ag nanoparticles. The Ag nanoparticles were strongly attached to the rGO so that 10 min ultrasonication of resulted nanocomposite was not able to decompose it. The stable 3D rGO/Ag nanocomposite showed the specific capacitance of about 845 F g^{-1} at 5 mV s^{-1} (876 F g^{-1} at 1 A g^{-1}). The presence of Ag nanoparticles accelerated the conductivity and faradic reactions and enhanced the accessible surface area that resulted in significant specific capacitance of 3D rGO/Ag nanocomposite. The prepared nanocomposite was able to keep about 97% of its capacitance after 1000 cycles at a scan rate of 100 mV s^{-1} . Due to the highly porous microstructure of 3D rGO, the ion diffusion length at the interfaces of 3D rGO/Ag nanocomposite electrode and the electrolyte was decrease and therefore the ion diffusion resistance was lowered.

Despite outstanding properties of 2D structured graphene nanosheets (2D GNSs), the π - π interaction and van der Waals attraction cause the restacking of 2D GNSs, which led to effective surface area reduction and destructive effect on their electrochemical properties.^[115] An effective procedure to overcome this

problem is the construction of 3D carbon-based aerogels.^[116] A 3D aerogel based on graphene/carbon nanotubes (GR-CNTs) was synthesized by Zhou et al.^[25b] via the freeze-drying process and usage of PVA as organic binder. The huge surface area, porous nanostructure, and supreme electrical conductivity were the prominent properties of the prepared 3D GR-CNTs aerogel. The electrochemical experiments revealed 375 F g^{-1} of specific capacitances in KOH solution, which retained 94.8% of its capacity after 5000 cycles. Also, the uniform formation of ultrafine Pt nanostructures on the 3D GR-CNTs aerogel introduced it as an appropriate support matrix for the construction of fuel cell electrodes. The obtained current density of 550 mA mg^{-1} with facilitated kinetics, high durability, and antifouling capacity for methanol electrocatalytic oxidation confirmed the applicability of the porous 3D GR-CNTs hybrid aerogel.

5. Conclusions and Future Perspective

Fabrication of porous materials with aligned micrometer-sized porosity and oriented structural elements is of importance for different applications, such as thermal insulation, pressure sensing, pollutant absorbent, and designing biomimetic scaffolds for tissue engineering. In this Review, we surveyed a generic, simple, and potent technique of directional freeze-casting method for the preparation of various 3D anisotropic porous materials, namely 3D open porous monoliths, films, fibers, and microparticles from the aqueous phase. In principle, the freeze-casting technique can be applied to a wide range of aqueous and nonaqueous-based slurries. However, in this

Review, we demonstrated solely the directional freeze-casting of the water-based carbonaceous components, water-soluble polymers, water-dispersible ceramic-based particles or 2D nano-sheets, as well as composite components as the principal building blocks of porous materials for different applications. Herein, very much depending on the freezing parameters, e.g., ice growth direction(s), freezing temperature and freezing rate, and concentration of slurry, various sophisticated array of complex microstructures with well-defined micrometer-sized porosities and aligned structure can be developed.

It is demonstrated that the preparation of aligned micrometer-sized porous materials is particularly advantageous for applications, such as thermal insulation with the purpose of thermal energy management. In this regard, the simultaneous anisotropic behavior in both thermal and mechanical behavior of the freeze-cast foams, obtained from their anisotropic microstructures, would be interesting for applications, such as thermal insulation in walls where the high strength in the axial direction and low thermal conductivity in the radial direction must be exploited. As the natural materials are a combination of lightness, strength, flexibility, and toughness, it seems that the freeze-casting approach can design materials with almost the same structural and mechanical features. In general, compared with the other sophisticated microfabrication techniques, such as self-assembly, layer-by-layer deposition, lithography, and 3D printing, the biomimetic behavior of directional freeze-casting technology offers a green way to fabricate various synthetic complex architectures from ceramics, polymers, and their composites. These synthetic structures in different length scales can emulate the hierarchical microstructuration, strengthening, and toughening mechanisms of natural materials, such as bone and nacre and plant stems. For example, the recent synthetic porous biomaterials with anisotropic alignment of micrometer-sized porosities through directional freeze-casting has indicated a great potential for bone tissue engineering, as it can mimic the microstructure of the bone tissue, and therefore, can act as a potent scaffold for bone tissue engineering with combination of biological cues, such as bioactive molecules and biological cells. The anisotropic scaffold structure developed by directional freeze-casting is a further asset for the cell guidance, differentiation, biofactor and nutrient delivery, and the bone vessel formations within the final scaffold. In addition, the bidirectional freeze-casting where the microstructures are directed with ice crystal growth through imposing thermal gradient in two directions, e.g., in radial and axial directions, is also reported as a highly suitable method to mimic the architecture of natural porous in synthetic aerogels. The generated biomimetic architecture with freeze-casting, namely lamellar layers with interconnected bridges, renders the aerogel with outstanding mechanical strength and resilience, which is usually very challenging to achieve with other hard templating techniques.

The compelling mechanical performance, together with lightweight and interconnected microarchitecture, make the developed aerogels/foams suitable for several other high-performance applications, such as pollutant absorption with high sorption efficiency, as well as in the construction of sensitive pressure sensor devices. In this regard, the developed architecture of porous aerogels with oriented pores can undergo large deformation and recover its initial shape even at high strains

without fracture or damage and therefore, can be utilized as a highly sensitive piezoresistive sensor for detecting the tiny pressure/strain caused, for example, by human body movements. It is also shown that for the pollutant absorption, the aligned micrometer-sized pores are responsible for maintaining the excellent mechanical performance of the composite as well as providing sufficient interspace for the absorption of the liquid- and gaseous-based pollutants.

Regarding energy storage and conversion application perspective, the aligned porous structure developed by directional freeze-casting is not crucial; however, in most of the relevant studies, this technique has been proposed as an effortless and straightforward technique with a purpose of fabrication of 3D open porous electrode structures with high electrical conductivity, mechanical resiliency, and physicochemical stability.

Finally, we hope that this Review encourages the use of directional freeze-casting for the preparation of new functional porous materials with a highly sophisticated microstructure. The success of this technique for controlling the shape and morphology at different levels is undoubtedly a reason for attracting a great deal of attention in recent years. Indeed, there is still much to investigate and to be fascinated by this processing technique to develop novel structures for different emerging applications where simultaneous control over the mechanical and microstructure properties is essential. To this end, the future hybridization of freeze-casting technology with the other advanced state of the art fabrication techniques, such as 3D-printing, microfluidic systems, and electrospinning is anticipated to create more sophisticated biomimetic designs of materials. It is expected that the future of materials' design mostly rely on the combination of aforementioned hybrid systems.

Acknowledgements

The majority of the text in this article has been drafted by H.M. H.M. would like to acknowledge the Department of Aerogel and Aerogel Composites of German Aerospace Center (DLR) as well as the Association of the Chemical Industry, the Chemical Industry Fund for the financial supports. Also, H.M. sincerely thanks Dr. Armeza Rege, Dr. Kathirvel Ganesan, and Prof. Dr. Barbara Milow from DLR for scientific discussions on tissue engineering, pressure sensing, and pollutants sorption application of freeze-cast aerogels and foams. M.-A.S. acknowledges the financial support from the Academy of Finland (grant no. 317316).

Conflict of Interest

The authors declare no conflict of interest.

Keywords

biomimetic materials design, directional freeze-casting, ice templating, materials fabrications, nanostructured 3D materials, porous nanomaterials, 3D monolithic aerogels

Received: January 9, 2020

Revised: March 18, 2020

Published online:

- [1] a) J. Ying, L. Lu, L. Tian, X. Yan, B. Chen, *Comput. Graphics* **2018**, 70, 157; b) A. Z. Lichtner, in *Anisotropic and Hierarchical Porosity in Multifunctional Ceramics*, University of Washington, ProQuest Dissertations Publishing **2015**, p. 3688931; c) H. Zhang, I. Hussain, M. Brust, M. F. Butler, S. P. Rannard, A. I. Cooper, *Nat. Mater.* **2005**, 4, 787.
- [2] X.-Y. Yang, L.-H. Chen, Y. Li, J. C. Rooke, C. Sanchez, B.-L. Su, *Chem. Soc. Rev.* **2017**, 46, 481.
- [3] A. Feinle, M. S. Elsaesser, N. Hüsing, *Chem. Soc. Rev.* **2016**, 45, 3377.
- [4] C. Triantafyllidis, M. S. Elsaesser, N. Hüsing, *Chem. Soc. Rev.* **2013**, 42, 3833.
- [5] C. Galassi, *J. Eur. Ceram. Soc.* **2006**, 26, 2951.
- [6] P. Colombo, C. Vakifahmetoglu, S. Costacurta, *J. Mater. Sci.* **2010**, 45, 5425.
- [7] a) M. Stucki, M. Loepfe, W. J. Stark, *Adv. Eng. Mater.* **2018**, 20, 1700611; b) J. Li, H. Ren, X. Zou, K. Cai, N. Zhao, G. Zhu, *Chem. Commun.* **2018**, 54, 8335; c) A. Rumpelcker, F. Kleitz, E.-L. Salabas, F. Schüth, *Chem. Mater.* **2007**, 19, 485.
- [8] J. Kim, V. Nese, J. Joos, K. Jeske, N. Duyckaerts, N. Pfänder, G. Prieto, *J. Mater. Chem. A* **2018**, 6, 21978.
- [9] T. Fukasawa, M. Ando, T. Ohji, S. Kanzaki, *J. Am. Ceram. Soc.* **2001**, 84, 230.
- [10] a) U. G. K. Wegst, H. Bai, E. Saiz, A. P. Tomsia, R. O. Ritchie, *Nat. Mater.* **2014**, 14, 23; b) M. C. Gutiérrez, M. L. Ferrer, F. del Monte, *Chem. Mater.* **2008**, 20, 634.
- [11] a) Q. Cheng, C. Huang, A. P. Tomsia, *Adv. Mater.* **2017**, 29, 1703155; b) M. M. Porter, J. McKittrick, M. A. Meyers, *JOM* **2013**, 65, 720.
- [12] S. R. Mukai, H. Nishihara, H. Tamon, *Chem. Com.* **2004**, 7, 874.
- [13] M. Klotz, I. Amirouche, C. Guizard, C. Viazzi, S. Deville, *Adv. Eng. Mater.* **2012**, 14, 1123.
- [14] W. Liao, H.-B. Zhao, Z. Liu, S. Xu, Y.-Z. Wang, *Composites, Part B* **2019**, 173, 107036.
- [15] S. Deville, *J. Mater. Res.* **2013**, 28, 2202.
- [16] S. Deville, *Adv. Eng. Mater.* **2008**, 10, 155.
- [17] C. Wang, X. Chen, B. Wang, M. Huang, B. Wang, Y. Jiang, R. S. Ruoff, *ACS Nano* **2018**, 12, 5816.
- [18] a) E. Munch, M. E. Launey, D. H. Alsem, E. Saiz, A. P. Tomsia, R. O. Ritchie, *Science* **2008**, 322, 1516; b) G. Lian, C.-C. Tuan, L. Li, S. Jiao, Q. Wang, K.-S. Moon, D. Cui, C.-P. Wong, *Chem. Mater.* **2016**, 28, 6096.
- [19] W. L. Li, K. Lu, J. Y. Walz, *Int. Mater. Rev.* **2012**, 57, 37.
- [20] K. L. Scotti, D. C. Dunand, *Prog. Mater. Sci.* **2018**, 94, 243.
- [21] S. Deville, *Materials* **2010**, 3, 1913.
- [22] a) B. P. Jelle, *Energy Build.* **2011**, 43, 2549; b) B. Wicklein, A. Kocjan, G. Salazar-Alvarez, F. Carosio, G. Camino, M. Antonietti, L. Bergström, *Nat. Nanotechnol.* **2014**, 10, 277.
- [23] Y. Li, H. Zhang, M. Fan, P. Zheng, J. Zhuang, L. Chen, *Sci. Rep.* **2017**, 7, 46379.
- [24] a) Z. Chen, Y. Hu, H. Zhuo, L. Liu, S. Jing, L. Zhong, X. Peng, R.-C. Sun, *Chem. Mater.* **2019**, 31, 3301; b) Y. Ding, T. Xu, O. Onyilagha, H. Fong, Z. Zhu, *ACS Appl. Mater. Interfaces* **2019**, 11, 6685.
- [25] a) Y. Zhou, J. Yang, C. Zhu, D. Du, X. Cheng, C. H. Yen, C. M. Wai, Y. Lin, *ACS Appl. Mater. Interfaces* **2016**, 8, 25863; b) Y. Zhou, X. C. Hu, S. Guo, C. Yu, S. Zhong, X. Liu, *Electrochim. Acta* **2018**, 264, 12.
- [26] a) A. Rigacci, J. C. Maréchal, M. Repoux, M. Moreno, P. Achard, *J. Non-Cryst. Solids* **2004**, 350, 372; b) Q. Peng, Y. Qin, X. Zhao, X. Sun, Q. Chen, F. Xu, Z. Lin, Y. Yuan, Y. Li, J. Li, W. Yin, C. Gao, F. Zhang, X. He, Y. Li, *ACS Appl. Mater. Interfaces* **2017**, 9, 44010; c) A. L. Moore, L. Shi, *Mater. Today* **2014**, 17, 163; d) J. Hu, Y. Huang, Y. Yao, G. Pan, J. Sun, X. Zeng, R. Sun, J.-B. Xu, B. Song, C.-P. Wong, *ACS Appl. Mater. Interfaces* **2017**, 9, 13544.
- [27] a) S. Wu, R. B. Ladani, J. Zhang, K. Ghorbani, X. Zhang, A. P. Mouritz, A. J. Kinloch, C. H. Wang, *ACS Appl. Mater. Interfaces* **2016**, 8, 24853; b) Y. Qin, Q. Peng, Y. Ding, Z. Lin, C. Wang, Y. Li, F. Xu, J. Li, Y. Yuan, X. He, Y. Li, *ACS Nano* **2015**, 9, 8933.
- [28] a) W. Zhan, S. Yu, L. Gao, F. Wang, X. Fu, G. Sui, X. Yang, *ACS Appl. Mater. Interfaces* **2017**, 10, 1093; b) S. Zhang, J. Sun, D. Hu, C. Xiao, Q. Zhuo, J. Wang, C. Qin, L. Dai, *J. Mater. Chem. A* **2018**, 6, 16139.
- [29] a) H. Maleki, M.-A. Shahbazi, S. Montes, S. H. Hosseini, M. R. Eskandari, S. Zaunschirm, T. Verwanger, S. Mathur, B. Milow, B. Krammer, N. Hüsing, *ACS Appl. Mater. Interfaces* **2019**, 11, 17256; b) M. Chau, K. J. De France, B. Kopera, V. R. Machado, S. Rosenfeldt, L. Reyes, K. J. W. Chan, S. Förster, E. D. Cranston, T. Hoare, E. Kumacheva, *Chem. Mater.* **2016**, 28, 3406.
- [30] E. Munch, E. Saiz, A. P. Tomsia, S. Deville, *J. Am. Ceram. Soc.* **2009**, 92, 1534.
- [31] B. Delattre, H. Bai, R. O. Ritchie, J. De Coninck, A. P. Tomsia, *ACS Appl. Mater. Interfaces* **2014**, 6, 159.
- [32] a) E. Munch, E. Saiz, A. P. Tomsia, S. Deville, *J. Am. Ceram. Soc.* **2009**, 92, 1534; b) S. M. Miller, X. Xiao, K. T. Faber, *J. Eur. Ceram. Soc.* **2015**, 35, 3595; c) S. W. Sofie, F. Dogan, *J. Am. Ceram. Soc.* **2001**, 84, 1459.
- [33] R. Li, X. Zhang, H. Dong, Q. Li, Z. Shuai, W. Hu, *Adv. Mater.* **2016**, 28, 1697.
- [34] a) K. G. Libbrecht, *Annu. Rev. Mater. Res.* **2017**, 47, 271; b) L. K. G. Youngster, *Eng. Sci.* **2001**, 64, 10.
- [35] S. Deville, J. Adrien, E. Maire, M. Scheel, M. Di Michiel, *Acta Mater.* **2013**, 61, 2077.
- [36] M. Marcellini, C. Noirjean, D. Dedovets, J. Maria, S. Deville, *ACS Omega* **2016**, 1, 1019.
- [37] K. Tai, Y. Liu, S. J. Dillon, *Microsci. Microanal.* **2014**, 20, 330.
- [38] P. Zhang, J. Li, L. Lv, Y. Zhao, L. Qu, *ACS Nano* **2017**, 11, 5087.
- [39] M. Yang, N. Zhao, Y. Cui, W. Gao, Q. Zhao, C. Gao, H. Bai, T. Xie, *ACS Nano* **2017**, 11, 6817.
- [40] J.-W. Moon, H.-J. Hwang, M. Awano, K. Maeda, *Mater. Lett.* **2003**, 57, 1428.
- [41] a) H. Bai, Y. Chen, B. Delattre, A. P. Tomsia, R. O. Ritchie, *Sci. Adv.* **2015**, 1, e1500849; b) H. Bai, F. Walsh, B. Gludovatz, B. Delattre, C. Huang, Y. Chen, A. P. Tomsia, R. O. Ritchie, *Adv. Mater.* **2016**, 28, 50.
- [42] Y. Tang, Q. Miao, S. Qiu, K. Zhao, L. Hu, *J. Eur. Ceram. Soc.* **2014**, 34, 4077.
- [43] W. Mahler, M. F. Bechtold, *Nature* **1980**, 285, 27.
- [44] D. W. Johnson, F. J. Schnettler, *J. Am. Cer. Soc.* **1970**, 53, 440.
- [45] M. Naviroj, S. M. Miller, P. Colombo, K. T. Faber, *J. Eur. Ceram. Soc.* **2015**, 35, 2225.
- [46] a) J. Lin, X. Yuan, G. Li, Y. Huang, W. Wang, X. He, C. Yu, Y. Fang, Z. Liu, C. Tang, *ACS Appl. Mater. Interfaces* **2017**, 9, 44732; b) X. Zeng, Y. Yao, Z. Gong, F. Wang, R. Sun, J. Xu, C.-P. Wong, *Small* **2015**, 11, 6205; c) X. Zeng, L. Ye, S. Yu, R. Sun, J. Xu, C.-P. Wong, *Chem. Mater.* **2015**, 27, 5849.
- [47] Y. Si, X. Wang, L. Dou, J. Yu, B. Ding, *Sci. Adv.* **2018**, 4, eaas8925.
- [48] H. Nishihara, S. R. Mukai, D. Yamashita, H. Tamon, *Chem. Mater.* **2005**, 17, 683.
- [49] H. Nishihara, S. R. Mukai, Y. Fujii, T. Tago, T. Masuda, H. Tamon, *J. Mater. Chem.* **2006**, 16, 3231.
- [50] C. Yu, J. Zhang, W. Tian, X. Fan, Y. Yao, *RSC Adv.* **2018**, 8, 21948.
- [51] a) Y. Qian, I. M. Ismail, A. Stein, *Carbon* **2014**, 68, 221; b) Y. Si, Q. Fu, X. Wang, J. Zhu, J. Yu, G. Sun, B. Ding, *ACS Nano* **2015**, 9, 3791.
- [52] a) Y.-Q. Li, Y. A. Samad, K. Polychronopoulou, S. M. Alhassan, K. Liao, *ACS Sustainable Chem. Eng.* **2014**, 2, 1492; b) Y. Ren, J. Zhang, Q. Xu, Z. Chen, D. Yang, B. Wang, Z. Jiang, *RSC Adv.* **2014**, 4, 23412; c) X.-L. Wu, T. Wen, H.-L. Guo, S. Yang, X. Wang, A.-W. Xu, *ACS*

- Nano* **2013**, *7*, 3589; d) Z.-Y. Wu, C. Li, H.-W. Liang, J.-F. Chen, S.-H. Yu, *Angew. Chem., Int. Ed.* **2013**, *52*, 2925.
- [53] a) L. Li, T. Hu, H. Sun, J. Zhang, A. Wang, *ACS Appl. Mater. Interfaces* **2017**, *9*, 18001; b) X. Yao, W. Yu, X. Xu, F. Chen, Q. Fu, *Nanoscale* **2015**, *7*, 3959.
- [54] Z. Wang, X. Shen, N. M. Han, X. Liu, Y. Wu, W. Ye, J.-K. Kim, *Chem. Mater.* **2016**, *28*, 6731.
- [55] a) X. Zhang, Z. Sui, B. Xu, S. Yue, Y. Luo, W. Zhan, B. Liu, *J. Mater. Chem.* **2011**, *21*, 6494; b) M. A. Worsley, P. J. Pauzauskie, T. Y. Olson, J. Biener, J. H. Satcher, T. F. Baumann, *J. Am. Chem. Soc.* **2010**, *132*, 14067.
- [56] Z. Chen, C. Xu, C. Ma, W. Ren, H.-M. Cheng, *Adv. Mater.* **2013**, *25*, 1296.
- [57] H. Sun, Z. Xu, C. Gao, *Adv. Mater.* **2013**, *25*, 2554.
- [58] a) Z. Chen, W. Ren, L. Gao, B. Liu, S. Pei, H.-M. Cheng, *Nat. Mater.* **2011**, *10*, 424; b) Z.-L. Wang, D. Xu, H.-G. Wang, Z. Wu, X.-B. Zhang, *ACS Nano* **2013**, *7*, 2422.
- [59] N. M. Han, Z. Wang, X. Shen, Y. Wu, X. Liu, Q. Zheng, T.-H. Kim, J. Yang, J.-K. Kim, *ACS Appl. Mater. Interfaces* **2018**, *10*, 6580.
- [60] a) G. Gorgolis, C. Galiotis, *2D Mater.* **2017**, *4*, 032001; b) Z. Xu, Y. Zhang, P. Li, C. Gao, *ACS Nano* **2012**, *6*, 7103.
- [61] M. A. Meyers, P.-Y. Chen, A. Y.-M. Lin, Y. Seki, *Prog. Mater. Sci.* **2008**, *53*, 1.
- [62] L. Qiu, J. Z. Liu, S. L. Y. Chang, Y. Wu, D. Li, *Nat. Commun.* **2012**, *3*, 1241.
- [63] T. Chen, J. Zhang, P. Shi, Y. Li, L. Zhang, Z. Sun, R. He, T. Duan, W. Zhu, *ACS Sustainable Chem. Eng.* **2018**, *6*, 17152.
- [64] X. Xie, Y. Zhou, H. Bi, K. Yin, S. Wan, L. Sun, *Sci. Rep.* **2013**, *3*, 2117.
- [65] J. Kim, J. Kim, S. Song, S. Zhang, J. Cha, K. Kim, H. Yoon, Y. Jung, K.-W. Paik, S. Jeon, *Carbon* **2017**, *113*, 379.
- [66] a) R. Okaji, K. Taki, S. Nagamine, M. Ohshima, *J. Appl. Polym. Sci.* **2012**, *125*, 2874; b) H. Liu, K. Nakagawa, D. Chaudhary, Y. Asakuma, M. O. Tadé, *Chem. Eng. Res. Des.* **2011**, *89*, 2356; c) F. Yokoyama, E. C. Achife, J. Momoda, K. Shimamura, K. Monobe, *Colloid Polym. Sci.* **1990**, *268*, 552; d) T. Köhnke, T. Elder, H. Theliander, A. J. Ragauskas, *Carbohydr. Polym.* **2014**, *100*, 24.
- [67] M. Barrow, H. Zhang, *Soft Matter* **2013**, *9*, 2723.
- [68] H. Kirsebom, G. Rata, D. Topgaard, B. Mattiasson, I. Y. Galaev, *Macromolecules* **2009**, *42*, 5208.
- [69] J. Wu, Q. Zhao, J. Sun, Q. Zhou, *Soft Matter* **2012**, *8*, 3620.
- [70] C. Rogers, D. Pun, Q. Fu, H. Zhang, *Ceramics* **2018**, *1*, 353.
- [71] Z. Wang, X. Shen, M. Akbari Garakani, X. Lin, Y. Wu, X. Liu, X. Sun, J.-K. Kim, *ACS Appl. Mater. Interfaces* **2015**, *7*, 5538.
- [72] A. Ouyang, A. Cao, S. Hu, Y. Li, R. Xu, J. Wei, H. Zhu, D. Wu, *ACS Appl. Mater. Interfaces* **2016**, *8*, 11179.
- [73] L. Estevez, A. Kellarakis, Q. Gong, E. H. Da'as, E. P. Giannelis, *J. Am. Chem. Soc.* **2011**, *133*, 6122.
- [74] K. A. Mauritz, R. B. Moore, *Chem. Rev.* **2004**, *104*, 4535.
- [75] Y. Shao, M. F. El-Kady, V. W. Lin, G. Zhu, K. L. Marsh, J. Y. Hwang, Q. Zhang, Y. Li, H. Wang, R. B. Kaner, *Adv. Mater.* **2016**, *28*, 6719.
- [76] a) J. T. McCann, D. Li, Y. Xia, *J. Mat. Chem.* **2005**, *15*, 735; b) I. G. Loscertales, A. Barrero, M. Márquez, R. Spretz, R. Velarde-Ortiz, G. Larsen, *J. Am. Chem. Soc.* **2004**, *126*, 5376; c) D. Li, A. Babel, S. A. Jenekhe, Y. Xia, *Adv. Mater.* **2004**, *16*, 2062.
- [77] M. Bognitzki, W. Czado, T. Frese, A. Schaper, M. Hellwig, M. Steinhart, A. Greiner, J. H. Wendorff, *Adv. Mater.* **2001**, *13*, 70.
- [78] J. T. McCann, M. Marquez, Y. Xia, *J. Am. Chem. Soc.* **2006**, *128*, 1436.
- [79] M.-H. Ho, P.-Y. Kuo, H.-J. Hsieh, T.-Y. Hsien, L.-T. Hou, J.-Y. Lai, D.-M. Wang, *Biomaterials* **2004**, *25*, 129.
- [80] a) R. Yu, Y. Shi, D. Yang, Y. Liu, J. Qu, Z.-Z. Yu, *ACS Appl. Mater. Interfaces* **2017**, *9*, 21809; b) A. Ouyang, C. Wang, S. Wu, E. Shi, W. Zhao, A. Cao, D. Wu, *ACS Appl. Mater. Interfaces* **2015**, *7*, 14439; c) S. Liao, T. Zhai, H. Xia, *J. Mater. Chem. A* **2016**, *4*, 1068.
- [81] J. Chaichanawong, K. Kongcharoen, S. Areerat, *Adv. Powder Technol.* **2013**, *24*, 891.
- [82] H. Cai, S. Sharma, W. Liu, W. Mu, W. Liu, X. Zhang, Y. Deng, *Biomacromolecules* **2014**, *15*, 2540.
- [83] S. Zhang, J. Sun, D. Hu, C. Xiao, Q. Zhuo, J. Wang, C. Qin, L. Dai, *J. Mater. Chem. A* **2018**, *6*, 16139.
- [84] K. Shu, C. Wang, S. Li, C. Zhao, Y. Yang, H. Liu, G. Wallace, *J. Mater. Chem. A* **2015**, *3*, 4428.
- [85] a) Y. Guo, K. Li, C. Hou, Y. Li, Q. Zhang, H. Wang, *ACS Appl. Mater. Interfaces* **2016**, *8*, 4676; b) E. Cuce, P. M. Cuce, C. J. Wood, S. B. Riffat, *Renewable Sustainable Energy Rev.* **2014**, *34*, 273.
- [86] a) N. Leventis, C. Chidambareswarapattar, D. P. Mohite, Z. J. Larimore, H. Lu, C. Sotiriou-Leventis, *J. Mater. Chem.* **2011**, *21*, 11981; b) M. D. Gawryla, M. Nezamzadeh, D. A. Schiraldi, *Green Chem.* **2008**, *10*, 1078.
- [87] a) S. T. Huxtable, D. G. Cahill, S. Shenogin, L. Xue, R. Ozisik, P. Barone, M. Usrey, M. S. Strano, G. Siddons, M. Shim, P. Keblinski, *Nat. Mater.* **2003**, *2*, 731; b) G. Pernot, M. Stoffel, I. Savic, F. Pezzoli, P. Chen, G. Savelli, A. Jacquot, J. Schumann, U. Denker, I. Mönch, C. Deneke, O. G. Schmidt, J. M. Rampoux, S. Wang, M. Plissonnier, A. Rastelli, S. Dilhaire, N. Mingo, *Nat. Mater.* **2010**, *9*, 491; c) M. D. Losego, I. P. Blitz, R. A. Vaia, D. G. Cahill, P. V. Braun, *Nano Lett.* **2013**, *13*, 2215.
- [88] a) J.-K. Yu, S. Mitrovic, D. Tham, J. Varghese, J. R. Heath, *Nat. Nanotechnol.* **2010**, *5*, 718; b) M. D. Losego, M. E. Grady, N. R. Sottos, D. G. Cahill, P. V. Braun, *Nat. Mater.* **2012**, *11*, 502.
- [89] a) R. Muthuraj, C. Jiménez-Saelices, Y. Grohens, B. Seantier, in *Biobased Aerogels: Polysaccharide and Protein-Based Materials* (Eds: S. Thomas, L. A. Pothan, R. Mavelil-Sam), Royal Society of Chemistry **2018**; b) S. Zhao, W. J. Malfait, N. Guerrero-Alburquerque, M. M. Koebel, G. Nyström, *Angew. Chem., Int. Ed.* **2018**, *57*, 7580.
- [90] a) H. Maleki, L. Whitmore, N. Hüsing, *J. Mater. Chem. A* **2018**, *6*, 12598; b) H. Maleki, S. Montes, N. Hayati-Roodbari, F. Putz, N. Huesing, *ACS Appl. Mater. Interfaces* **2018**, *10*, 22718.
- [91] a) N. Zanjanzadeh Ezazi, M.-A. Shahbazi, Y. V. Shatalin, E. Nadal, E. Mäkilä, J. Salonen, M. Kemell, A. Correia, J. Hirvonen, H. A. Santos, *Int. J. Appl. Pharm.* **2018**, *536*, 241; b) S. Pina, V. P. Ribeiro, C. F. Marques, F. R. Maia, T. H. Silva, R. L. Reis, J. M. Oliveira, *Materials* **2019**, *12*, 1824; c) C. D. Spicer, *Polym. Chem.* **2020**, *11*, 184.
- [92] L. Polo-Corrales, M. Latorre-Esteves, J. E. Ramirez-Vick, *J. Nanosci. Nanotechnol.* **2014**, *14*, 15.
- [93] a) A. Rouhollahi, O. Ilegbusi, S. Florczyk, K. Xu, H. Foroosh, *Ann. Biomed. Eng.* **2019**, *48*, 1090; b) I. Bružauskaitė, D. Bironaitė, E. Bagdonas, E. Bernotienė, *Cytotechnology* **2016**, *68*, 355; c) U. Stachewicz, P. K. Szewczyk, A. Kruk, A. H. Barber, A. Czyska-Filemonowicz, *Mater. Sci. Eng. C* **2019**, *95*, 397.
- [94] a) L. Che, Z. Lei, P. Wu, D. Song, *Adv. Powder Technol.* **2019**, *29*, 1904450; b) J. C. Lee, E. J. Volpicelli, *Adv. Healthcare Mater.* **2017**, *6*, 1700232; c) M. Ghosh, M. Halperin-Sternfeld, I. Grinberg, L. Adler-Abramovich, *Nanomaterials* **2019**, *9*, 497.
- [95] a) P. Divakar, K. Yin, U. G. K. Wegst, *J. Mech. Behav. Biomed. Mater.* **2019**, *90*, 350; b) M. Schardosim, J. Soulié, D. Poquillon, S. Cazalbou, B. Duployer, C. Tenaillon, C. Rey, R. Hübler, C. Combes, *Mater. Sci. Eng. C* **2017**, *77*, 731; c) Y. Huang, S. Onyeri, M. Siewe, A. Moshfeghian, S. V. Madhally, *Biomaterials* **2005**, *26*, 7616; d) H. Schoof, L. Bruns, A. Fischer, I. Heschel, G. Rau, *J. Cryst. Growth* **2000**, *209*, 122; e) S. Stokols, M. H. Tuszynski, *Biomaterials* **2004**, *25*, 5839; f) W. Tao, M. Li, R. Xie, *Macromol. Mater. Eng.* **2005**, *290*, 188; g) L. Shapiro, S. Cohen, *Biomaterials* **1997**, *18*, 583; h) S. Zmora, R. Glicklis, S. Cohen, *Biomaterials* **2002**, *23*, 4087; i) A. Tampieri, M. Sandri, E. Landi, G. Celotti, N. Roveri, M. Mattioli-Belmonte, L. Virgili, F. Gabbanelli, G. Biagini, *Acta Biomater.* **2005**, *1*, 343.

- [96] D. M. M. dos Santos, S. M. de Carvalho, M. M. Pereira, M. Houmard, E. H. M. Nunes, *Crearm. Int.* **2019**, *45*, 9891.
- [97] Y. Tian, K. Liang, X. Wang, Y. Ji, *ACS Sustainable Chem. Eng.* **2017**, *5*, 3305.
- [98] D. Wang, F. Romer, L. Connell, C. Walter, E. Saiz, S. Yue, P. D. Lee, D. S. McPhail, J. V. Hanna, J. R. Jones, *J. Mater. Chem. B* **2015**, *3*, 7560.
- [99] a) D. Motlagh, J. Allen, R. Hoshi, J. Yang, K. Lui, G. Ameer, *J. Biomed. Mater. Res., Part A* **2007**, *82A*, 907; b) Y. Kang, J. Yang, S. Khan, L. Anissian, G. A. Ameer, *J. Biomed. Mater. Res., Part A* **2006**, *77A*, 331; c) A. K. Sharma, P. V. Hota, D. J. Matoka, N. J. Fuller, D. Jandali, H. Thaker, G. A. Ameer, E. Y. Cheng, *Biomaterials* **2010**, *31*, 6207; d) J. Tang, *J. Mater. Chem. B* **2015**, *3*, 5569.
- [100] J. C. Courtenay, J. G. Filgueiras, E. R. deAzevedo, Y. Jin, K. J. Edler, R. I. Sharma, J. L. Scott, *J. Mater. Chem. B* **2019**, *7*, 53.
- [101] Y. Ma, Y. Yue, H. Zhang, F. Cheng, W. Zhao, J. Rao, S. Luo, J. Wang, X. Jiang, Z. Liu, N. Liu, Y. Gao, *ACS Nano* **2018**, *12*, 3209.
- [102] N. Zhao, M. Yang, Q. Zhao, W. Gao, T. Xie, H. Bai, *ACS Nano* **2017**, *11*, 4777.
- [103] Y. Zang, F. Zhang, C.-A. Di, D. Zhu, *Mater. Horizons* **2015**, *2*, 140.
- [104] a) H. Huang, P. Chen, X. Zhang, Y. Lu, W. Zhan, *Small* **2013**, *9*, 1397; b) Y. Xu, K. Sheng, C. Li, G. Shi, *ACS Nano* **2010**, *4*, 4324; c) M. B. Bryning, D. E. Milkie, M. F. Islam, L. A. Hough, J. M. Kikkawa, A. G. Yodh, *Adv. Mater.* **2007**, *19*, 661; d) M. A. Worsley, P. J. Pauzauskie, T. Y. Olson, J. Biener, J. H. Satcher, T. F. Baumann, *J. Am. Chem. Soc.* **2010**, *132*, 14067.
- [105] J. Zou, J. Liu, A. S. Karakoti, A. Kumar, D. Joung, Q. Li, S. I. Khondaker, S. Seal, L. Zhai, *ACS Nano* **2010**, *4*, 7293.
- [106] J. Kuang, Z. Dai, L. Liu, Z. Yang, M. Jin, Z. Zhang, *Nanoscale* **2015**, *7*, 9252.
- [107] Y. Tang, *J. Mater. Chem. A* **2013**, *1*, 6723.
- [108] a) H. Maleki, *Chem. Eng. J.* **2016**, *300*, 98; b) H. Maleki, N. Hüsing, *Appl. Catal., B* **2018**, *221*, 530.
- [109] W. Tanthapanichakoon, H. Tamon, K. Nakagawa, T. Charinpanitkul, *Eng. J.* **2013**, *17*, 1.
- [110] S. Deville, *Adv. Eng. Mater.* **2008**, *10*, 155.
- [111] a) K. H. Lee, Y. W. Lee, S. W. Lee, J. S. Ha, S. S. Lee, J. G. Son, *Sci. Rep.* **2015**, *5*, 13696; b) K. Y. Yoon, J. S. Lee, K. Kim, C. H. Bak, S. I. Kim, J. B. Kim, J. H. Jang, *ACS Appl. Mater. Interfaces* **2014**, *6*, 22634; c) C. Hu, Z. Mou, G. Lu, N. Chen, Z. Dong, M. Hu, L. Qu, *Phys. Chem. Chem. Phys.* **2003**, *15*, 13038.
- [112] a) Y. Tang, Y. Zhang, J. Deng, D. Qi, W. R. Leow, J. Wei, S. Yin, Z. Dong, R. Yazami, Z. Chen, X. S. Chen, *Angew. Chem., Int. Ed.* **2014**, *53*, 13488; b) Y. Tang, Y. Zhang, J. Deng, J. Wei, H. L. Tam, B. K. Chandran, Z. Dong, Z. Chen, X. Chen, *Adv. Mater.* **2014**, *26*, 6111; c) Y. Tang, J. Deng, W. Li, O. I. Malyi, Y. Zhang, X. Zhou, S. Pan, J. Wei, Y. Cai, Z. Chen, X. Chen, *Adv. Mater.* **2017**, *29*, 1701828.
- [113] H. D. Jang, S. K. Kim, H. Chang, J. H. Choi, B. G. Cho, E. H. Jo, J. W. Choi, J. Huang, *Carbon* **2015**, *93*, 869.
- [114] P. K. Sahoo, N. Kumar, S. Thiyagarajan, D. Thakur, H. S. Panda, *ACS Sustainable Chem. Eng.* **2018**, *6*, 7475.
- [115] J. Luo, H. D. Jang, T. Sun, L. Xiao, Z. He, A. P. Katsoulidis, J. Huang, *ACS Nano* **2011**, *5*, 8943.
- [116] Y. Zhou, X. C. Hu, Q. Fan, H. R. Wen, *J. Mater. Chem* **2016**, *4*, 4587.